remote sensing

MDPI

Article

Estimation of Biochemical Compounds in Tradescantia Leaves Using VIS-NIR-SWIR Hyperspectral and Chlorophyll a Fluorescence Sensors

Renan Falcioni [1,*], Roney Berti de Oliveira [1], Marcelo Luiz Chicati [1], Werner Camargos Antunes [1], José Alexandre M. Demattê [2] and Marcos Rafael Nanni [1]

[1] Department of Agronomy, State University of Maringá, Av. Colombo, 5790, Maringá 87020-900, Paraná, Brazil; rboliveira@uem.br (R.B.d.O.); mlchicati@uem.br (M.L.C.); wcantunes@uem.br (W.C.A.); mrnanni@uem.br (M.R.N.)

[2] Department of Soil Science, Luiz de Queiroz College of Agriculture, University of São Paulo, Av. Pádua Dias, 11, Piracicaba 13418-260, São Paulo, Brazil; jamdemat@usp.br

* Correspondence: renanfalcioni@gmail.com or rfalcioni2@uem.br; Tel.: +55-4430118940

Abstract: An integrated approach that utilises hyperspectral and chlorophyll a fluorescence sensors to predict biochemical and biophysical parameters represents a new generation of remote-sensing research. The main objective of this study was to obtain a detailed spectral profile that correlates with plant physiology, thereby enhancing our understanding and management of plant health, pigment profiles, and compound fingerprints. Leveraging datasets using non-imaging or passive hyperspectral and chlorophyll fluorescence sensors to collect data in Tradescantia species demonstrated significant differences in leaf characteristics with pigment concentrations and structural components. The main goal was to use principal component analysis (PCA) and partial least squares regression (PLS) methods to analyse the variations in their spectra. Our findings demonstrate a strong correlation between hyperspectral data and chlorophyll fluorescence, which is further supported by the development of hyperspectral vegetation indices (HVIs) that can accurately evaluate fingerprints and predict many compounds in variegated leaves. The higher the integrated analytical approach and its potential application in HVIs and fingerprints, the better the selection of wavelengths and sensor positions for rapid and accurate analysis of many different compounds in leaves. Nonetheless, limitations arose from the specificity of the data for the Tradescantia species, warranting further research across diverse plant types and compounds in the leaves. Overall, this study paves the way for more sustainable and informed agricultural practices through breakthroughs in the application of sensors to remote-sensing technologies.

Keywords: biochemical compounds; HVI; hyperspectral sensors; partial least squares regression; principal component analysis; purple leaves

Citation: Falcioni, R.; Oliveira, R.B.d.; Chicati, M.L.; Antunes, W.C.; Demattê, J.A.M.; Nanni, M.R. Estimation of Biochemical Compounds in Tradescantia Leaves Using VIS-NIR-SWIR Hyperspectral and Chlorophyll a Fluorescence Sensors. *Remote Sens.* **2024**, *16*, 1910. https://doi.org/10.3390/rs16111910

Academic Editors: Jonghan Ko, Wei Xue and Xinwei Li

Received: 30 April 2024
Revised: 22 May 2024
Accepted: 24 May 2024
Published: 26 May 2024

1. Introduction

The integration of hyperspectral sensors with chlorophyll fluorescence techniques represents a significant advancement in leaf signature analysis [1]. These cutting-edge methodologies provide a detailed understanding of the physiological and biochemical states of vegetation, enabling us to understand plant responses to various environmental conditions [2,3]. These tools not only improve the accuracy of traditional assessments but also open up new possible innovative approaches for monitoring plant health and managing agriculture [4–6].

Chlorophyll fluorescence (ChlF) curves are an essential tool for assessing plant health because they allow for the accurate mapping of pigment concentrations and biochemical components based on 1 s curves [7,8]. By measuring the fluorescence emitted by chlorophyll a, these curves provide valuable insights into the photosynthetic efficiency and stress response of plants. The data obtained from the ChlF curves can reveal variations in chlorophyll content, as well as changes in other pigments and biochemical markers, which are crucial for understanding the physiological state of the plant [9–11]. This technique is particularly useful for detecting early signs of stress before visible symptoms appear, enabling proactive management and mitigation strategies for crop cultivation and environmental monitoring or pigment profiling in leaves [12,13].

Hyperspectral curves derived from both imaging and non-imaging sensors provide a comprehensive spectral profile of plant leaves and capture detailed information over a wide range of wavelengths [14–17]. Non-imaging hyperspectral sensors offer distinct advantages. These sensors facilitate rapid data acquisition without the need for spatial context, making them highly efficient for large-scale or remote assessments. The flexibility and precision of non-imaging hyperspectral sensors enable the detection of subtle physiological changes, enhancing the capacity to monitor plant stress responses with exceptional accuracy [11,18–21]. Consequently, these tools are invaluable for advancing our understanding of plant dynamics and improving agricultural practices.

With the intricate cellular and foliar architecture of plants, an array of chloroplastic pigments, such as chlorophylls and carotenoids, and non-chloroplastic compounds, including anthocyanins, flavonoids, and phenolic compounds, have been identified [22–24]. Moreover, structural components such as lignin and cellulose play critical roles in the biomechanical integrity of plant tissues. The concentrations of these biochemical constituents can vary significantly and are influenced by factors such as the expansion of leaf area, leaf thickness, and the number and structural alterations of cells [21,23,25]. These variations are pivotal because they reflect the biophysical and biochemical dynamics within the plant and offer insights into its adaptive responses to environmental conditions.

Principal component analysis (PCA) is an advanced statistical method that is widely applied to address the complexity and high dimensionality of hyperspectral and fluorescence data [22,26–28]. This method effectively separates and recognises patterns by reducing data dimensionality while maintaining most of the variance, thus revealing the underlying variability among the samples. One of the main benefits of PCA is its ability to select the optimal number of principal components (PCs) required to capture significant data features [27,29,30]. This choice is vital because it balances the maximisation of information retention with minimising noise. The β-loadings obtained from PCA provide a clear illustration of the spectral peaks, offering "fingerprints" of the chemical and physical properties within the dataset [22,23]. Furthermore, PCA can be combined with regression coefficients obtained from various spectral curves, such as OJIP, which represent the fluorescence kinetics over the first few seconds of illumination, and hyperspectral reflectance, transmittance, and absorbance curves. This combination allows for more comprehensive analysis by combining biochemical and biophysical insights [31]. Such a multifaceted approach enhances the understanding of plant responses and interactions with their environment, aiding in more accurate and predictive modelling of plant physiology and agronomy by remote-sensing techniques [4–6,32].

Hyperspectral vegetation indices (HVIs) are useful for analysing large datasets from both chlorophyll fluorescence and hyperspectral measurements [15,33–35]. By simplifying complex spectral data into understandable indices, HVIs enable the effective large-scale surveillance and mapping of more relevant parameters. These indices can be used to systematically identify areas of specific interest wavelengths by locating regions of interest in which key biochemical and biophysical components or fingerprint indicators show significant changes [22,23]. For example, specific HVIs can be designed to detect changes in chlorophyll content, water stress, and nutrient levels [25,29,36–38]. The combination of these indices with chlorophyll fluorescence data improves the ability to spatially differentiate areas with different photosynthetic efficiencies or stress reactions, whereas hyperspectral data can be used to map the distribution of various biochemical markers across a landscape. Ultimately, the application of HVIs provides a powerful tool for precision agriculture and environmental monitoring. By converting complex spectral data into actionable information, these indices enable the development of targeted intervention strategies, maximisation of resource use, and improvement of crop management practices.

Partial least squares regression (PLSR) is a general method for analysing hyperspectral data for predictive modelling because it can effectively handle highly collinear and multivariate data [22,26,27,39,40]. This method is particularly useful when there are more predictor variables than observations, which is often the case in spectral analysis. PLSR works by finding the most relevant information from the predictors (in this case, spectral bands) by projecting them onto a new subspace defined by the latent variables. These latent variables are selected not only for their ability to account for the variance in the predictors but also for their correlation with the response variable, which is essential for making accurate predictions [27,40,41]. One of the main benefits of PLSR is its ability to handle multicollinearity among spectral bands well, where traditional regression methods may not work or yield unreliable coefficients. PLSR reduces the predictors to a smaller set of uncorrelated components while maintaining the ability to capture key patterns related to the response variable.

PLSR is useful not only for prediction but also for exploratory data analysis as it can uncover hidden patterns and associations in the data. It can be very effective when combined with other techniques, such as cross-validation, to increase model stability and assess predictive performance [27,42]. PLSR stands out for its flexibility and efficiency in dealing with complex and large datasets that are common in hyperspectral imaging, making it a preferred method for both academic research and practical applications in fields such as remote sensing, chemometrics, and precision agriculture [27,40,41]. For those who want to know more about this method, detailed applications and comparisons with other techniques are often found in the scientific literature related to spectroscopy and data analysis [22,26,27,39,40].

This study aimed to improve the prediction of chlorophyll a fluorescence parameters together using hyperspectral sensors. The main objective of this study was to identify specific spectral bands by HVI using hyperspectral data that are strongly correlated with chlorophyll a fluorescence to aid in the estimation of seventeen biochemical and biophysical parameters in Tradescantia plants. This concerns considering the shape of leaf structures, which is relevant to plant physiology. The hypothesis of this study is that by combining and enhancing the use of advanced hyperspectral sensors for reflectance, transmittance, and absorbance data, along with powerful multivariate statistical methods such as PCA and PLSR, it is possible to increase the prediction of these data parameters (Figure 1).

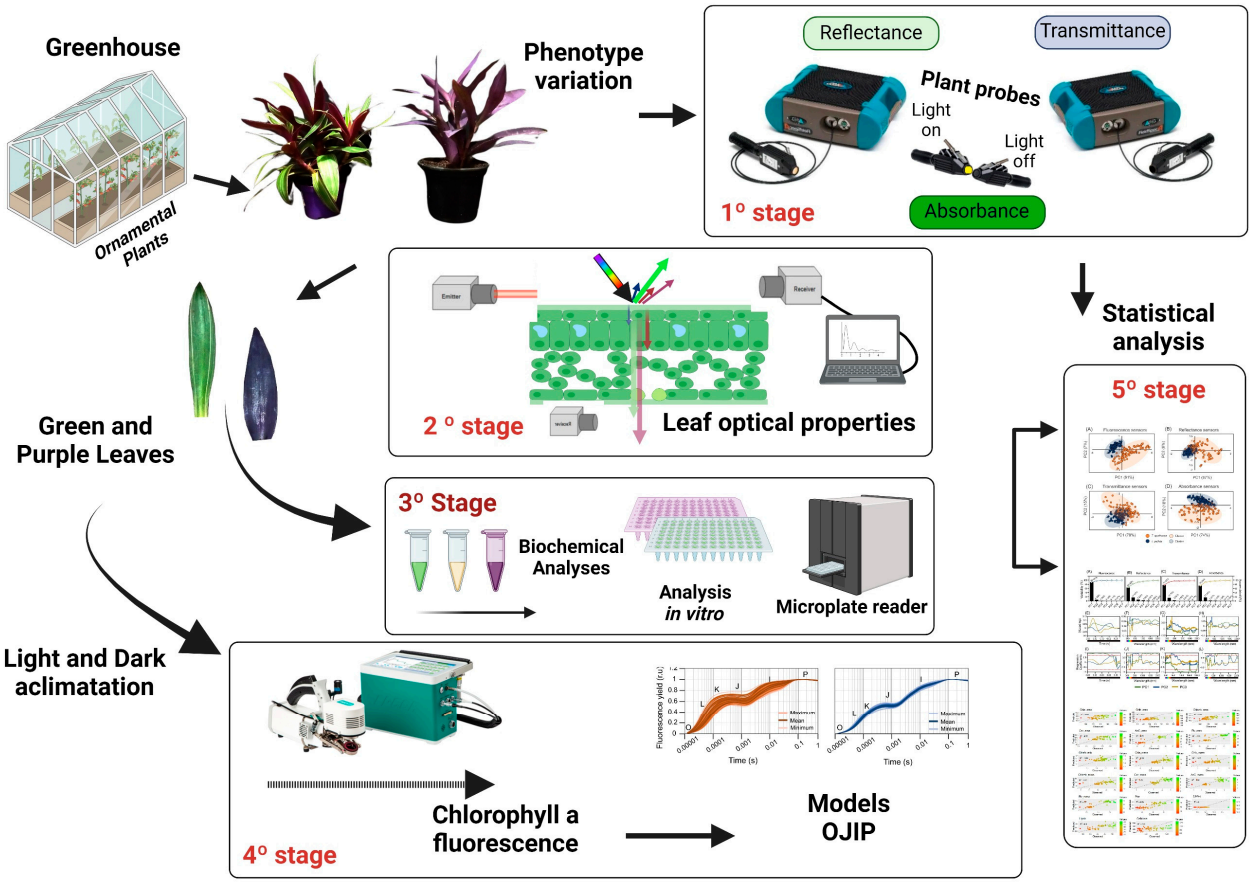

Figure 1. A flowchart showing how to predict the biochemical compounds in *Tradescantia spathacea* (L.) Olof Swartz and *Tradescantia pallida* (Rose) D.R. Hunt. plants, using two hyperspectral and chlorophyll sensors. Stage 1 involved growing plants in a greenhouse and using two hyperspectral sensors to measure the reflectance, transmittance, and absorbance spectra of their leaves. Stage 2 involves examining leaves to detect changes in their optical properties. In Stage 3, the levels of biochemical compounds in the leaves were measured using a microplate reader. In Stage 4, the leaves were exposed to dark conditions to measure chlorophyll a fluorescence and evaluate the prediction models. Stage 5 involves analysing the data using PLS and other multivariate statistical methods for the classification and prediction of biochemical and biophysical parameters. Created with BioRender.com.

2. Materials and Methods

2.1. Plant Materials and Experimental Design

The model plants *Tradescantia spathacea* (L.) Olof Swartz and *Tradescantia pallida* (Rose) D.R. Hunt., plants that exhibit variations in pigment concentration and leaf thickness, were cultivated in 2 L pots at the Botanical Garden of the State University of Maringá, Brazil. These plants were grown under greenhouse conditions, benefiting from natural light, and maintained within a temperature range of 22 °C to 26 °C under a 16-h photoperiod. Regular watering was conducted twice daily, at 8 a.m. and 6 p.m., to ensure consistent hydration. Leaves of various ages and positions (apex, middle, and base) were sampled from different sections of the plants. The investigation involved hyperspectral reflectance analysis and leaf biochemical profiling of a total of 200 samples. All measurements were meticulously performed between 11 a.m. and 1 p.m. to maintain consistency in the data collection. A summary of the analytical procedure is shown in Figure 1.

2.2. OJIP Chlorophyll a Fluorescence Transient

The leaves were analysed using an infrared gas exchange analyser (IRGA) with a Multiphase Flash^{TM} Fluorometer (LI-6800-01; LI-COR Inc., Lincoln, NE, USA) equipped with a constant concentration of 400 µmol mol^{-1} in the chamber sample (CO_2_sample) and a relative humidity of 60% in the sample chamber (%RH_sample). A flow rate of 700 µmol s^{-1}, a fan speed of 10,000 rpm, and a sample heat exchanger temperature of 25 °C were maintained within a 6 cm^2 sample chamber. The sensor operates at >720 nm, specifically for chlorophyll a fluorescence [23].

To elicit chlorophyll a fluorescence transients, the leaves were subjected to dark acclimation for 12 h in the dark. Thereafter, a clipping chamber was used, and a saturating light pulse of 15,000 µmol m^{-2} s^{-1} was applied for 1 s in induction mode, ensuring the closure of all reaction centres [13].

2.3. Hyperspectral Optical Leaf Properties

A FieldSpec® 3 spectroradiometer with an ASD Contact PlantProbe® (ASD Inc., Boulder, CO, USA) with a diameter of 10 mm was used to measure the reflectance (R) and transmittance (T) of the leaves. The equipment consisted of a VNIR detector with a 512-element silicon array for wavelengths ranging from 350 to 1000 nm (3 nm spectral resolution), an SWIR 1 detector with a Graded Index InGaAs Photodiode, a Two-Stage TE Cooled for wavelengths from 1001 to 1800 nm (10 nm spectral resolution), an SWIR 2 detector with a Graded Index InGaAs Photodiode, and a Two-Stage TE Cooled for wavelengths from 1801 to 2500 nm (10 nm spectral resolution), with interpolation in 1 nm by spectroradiometer equipment. This spectroradiometer is based on non-imaging passive sensors. A PlantProbe® leaf clip was used to minimise atmospheric effects. ViewSpec Pro software version 6.2 (ASD Inc., Boulder, CO, USA) was used to preprocess the data and change the sensor at 1000 and 1800 nm. Standard white reference plates were used to calibrate and optimise the equipment. A high-intensity light beam (1500 µmol m^{-2} s^{-1}) was measured at 1 cm from the light source with an irradiance sensor measured by LI-180 (LI-COR Inc., Lincoln, NE, USA), and from one plant probe was directed to the upper (adaxial) surface of the leaf, whereas another probe, without its light beam, assessed the lower (abaxial) surface of the leaf. The reflectance and transmittance for each wavelength were recorded simultaneously, and the absorbance was calculated using the formula [A = 1 − (R + T)].

2.4. Evaluation of Biochemical and Biophysical Leaf Tissue Composition

2.4.1. Measurement of Chlorophyll and Carotenoid Contents

We used a modified version of the method by Gitelson and Solovchenko (2018) [43] to determine the concentrations of chlorophyll *a*, chlorophyll *b*, total chlorophyll (*a*+*b*), and carotenoids, including carotenes and xanthophylls. The absorbance of the methanol extract from the apolar phase of chloroform:methanol (2:1) extraction was measured at 470, 652, and 665 nm [44]. We calculated the concentrations of these pigments using these formulas and expressed the final concentrations in mg cm^{-2} and mg g^{-1} [44].

2.4.2. Measurement of Anthocyanins and Flavonoids

To measure anthocyanins, we acidified the water-methanol phase with hydrochloric acid and measured its absorbance at λ530 nm using the molar absorption coefficient of Gitelson and Solovchenko (2018) [43]. To measure flavonoids, we examined the polar fraction of the methanol extract at a wavelength of 358 nm. We also used molar absorption coefficients according to the method described by Gitelson and Solovchenko (2018) [43].

2.4.3. Evaluation of Antioxidant Capacity

To measure the total antioxidant capacity of the samples, we followed a modified version of the DPPH assay, based on the method described by Llorach et al. (2008) [45]. In this assay, we incubated the methanolic extract with 1 mM DPPH solution and recorded the absorbance of the mixture for colour changes.

2.4.4. Measurement of Phenolic Compounds in Leaves

We used a modified version of the method described by Ragaee (2006) [46] to measure the soluble phenolic compounds. The methanolic extract was mixed with Folin–Ciocalteu reagent, sodium carbonate (Na_2CO_3), and deionised water. The mixture was incubated in the dark and centrifuged to separate the phases. The absorbance of the supernatant was measured at a wavelength of 725 nm.

2.5. Hyperspectral Vegetation Indices Using Optimal Wavelengths for JIP-Test and Hyperspectral Parameters

The hyperspectral bands and chlorophyll a fluorescence were calculated using the normalised difference vegetation index formula (Equation (1)), as outlined by Crusiol et al. (2023) [27]. This procedure yielded unique hyperspectral vegetation indices (HVIs). Each HVI was then correlated with relevant cross-sections pertaining to chlorophyll a kinetic parameters. These correlations were quantified using the Pearson correlation coefficient and the coefficient of determination (R^2) using a custom IDL code. The data were collected using a ground-based sensor, which captured spectra across a range of 350–2500 nm, and the results are presented in a contour map.

$$HVI = \frac{Wavelength\ 1 - Wavelength\ 2}{Wavelength\ 1 + Wavelength\ 2} \quad (1)$$

2.6. Partial Least Squares Regression (PLSR) by Analysis of Spectroscopy Data

The hyperspectral data were centred on the mean and subjected to PLSR to create prediction models for JIP test parameters. To achieve this, the spectral data of the various parameters of the 200 samples were divided into two groups: 75% (150) of the samples were allocated to the training group, whereas the remaining 25% (50) were designated as the prediction group. This allocation was chosen to ensure that the resulting estimates were valid and accurate. Validity was ensured by preventing an overestimation of the accuracy, which was maximised by minimising the overestimation of the approximation error. This approach was based on the analysis described in [22,23].

Calibration (Cal) and cross-validation (Cva) were employed to predict quality attributes based on the JIP test. Furthermore, the predictive capabilities of the calibration model were assessed by calculating metrics, such as the coefficient of determination. (R^2; $1 - \frac{SS_{res}}{SS_{tot}}$), offset, root mean square error (RMSE; $\sqrt{\sum_{i=1}^{n} \frac{(\hat{Y}i - Yi)^2}{n}}$), the ratio of performance to deviation (RPD; $\frac{1}{\sqrt{1-R_x^2}}$), and bias were used to assess the quality, precision, and accuracy of the model, as described in [23].

2.7. Statistical Analyses

2.7.1. Descriptive, Univariate, and Multivariate Statistical Analyses

Descriptive statistics were used to describe the biochemical parameters. For each parameter, assessments included the count (n), mean, median, minimum, maximum, and coefficient of variation (CV, %). The CV was categorised according to the criteria proposed by Zar (2010) [47]. Pearson's correlation methodology was employed to determine the interrelationships between biochemical and biophysical attributes. For these analytical tasks, we utilised Statistica 10® (StatSoft Inc., Tulsa, OK, USA) and the R-Studio software version 2023.12.1 (Posit Software, PBC, Boston, MA, USA) framework. Graphical representations were generated using a range of applications: SigmaPlot 10.0® (Systat Inc., Santa Clara, Silicon Valley, CA, USA), R-Studio software, Excel 365 version 2404 (Microsoft Inc., Silicon Valley, CA, USA), and CorelDraw 2024® version 25 (Corel Corp., Ottawa, ON, Canada).

2.7.2. Principal Component Analysis (PCA)

Unscrambler X software, version 10.4 (CAMO Software, Oslo, Norway), was used for principal component analysis (PCA) of the growth parameter data. This was achieved with a predetermined statistical significance level of $p < 0.01$. To ensure that the analysis was not subject to underfitting or overfitting, the optimal number of principal components was determined based on the first maximum value of overall accuracy, as outlined in [22,23].

3. Results

3.1. Statistical Description of the Biochemical Compounds

Table 1 provides a comprehensive statistical analysis of various biochemical compounds measured in the leaves of *Tradescantia spathacea* (L.) Olof Swartz and *Tradescantia pallida* (Rose) D.R. Hunt., species based on 200 samples per parameter. The data included the mean, median, minimum, maximum, and coefficient of variation for each compound (Table 1).

Table 1. The descriptive statistics of biochemical compound parameters measured in the leaves of *Tradescantia spathacea* (L.) Olof Swartz and *Tradescantia pallida* (Rose) D.R. Hunt. species. For each parameter, data were collected for 200 samples, including the mean, median, minimum, and maximum values and the coefficient of variation (CV%). (n = 200).

Parameter	Count (n)	Mean	Median	Minimum	Maximum	CV (%)
Chl*a* (mg m^{-2})	200	765.25	760.47	480.20	996.52	10.92
Chl*b* (mg m^{-2})	200	487.48	469.65	262.06	875.10	18.99
Chl*a*+*b* (mg m^{-2})	200	1252.73	1231.39	742.26	1871.61	13.89
Car (mg m^{-2})	200	263.54	264.23	185.89	362.00	9.24
AnC (nmol cm^{-2})	200	23.78	23.59	18.36	27.48	6.52
Flv (nmol cm^{-2})	200	34.02	32.94	17.97	51.74	18.21
Chl*a*/*b* ratio	200	1.59	1.61	1.14	1.94	7.63
Chl*a* (mg g^{-1})	200	10.53	10.30	0.96	17.50	28.99
Chl*b* (mg g^{-1})	200	6.64	6.85	0.64	11.77	29.01
Chl*a*+*b* (mg g^{-1})	200	17.16	17.46	1.60	27.88	28.68
Car (mg g^{-1})	200	3.64	3.57	0.33	6.40	29.58
AnC (µmol g^{-1})	200	3.37	2.92	0.24	5.75	37.07
Flv (µmol g^{-1})	200	4.94	3.75	0.33	11.32	46.51
Phe (mL L^{-1})	200	57.91	57.59	29.02	111.31	29.66
DPPH	200	91.73	91.68	88.58	99.30	1.35
Lignin (mg g^{-1})	200	307.67	303.22	178.09	422.13	19.68
Cellulose (nmol mg^{-1})	200	725.52	671.16	322.95	1386.90	37.39

Chlorophyll *a* (Chl*a*, mg m^{-2}) had a mean of 765.25, a median of 760.47, a minimum of 480.20, and a maximum of 996.52, with a coefficient of variation of 10.92%. Chlorophyll *b* (Chl*b*, mg m^{-2}) had a mean of 487.48, a median of 469.65, a minimum of 262.06, and a maximum of 875.10, with a high variation coefficient of 18.99%. Total chlorophyll *a*+*b* (Chl*a*+*b*, mg m^{-2}) had a mean of 1252.73, a median of 1231.39, a minimum of 742.26, and a maximum of 1871.61, with a variation coefficient of 13.89%. Carotenoids (Car, mg m^{-2}) had a mean of 263.54, a median of 264.23, a minimum of 185.89, and a maximum of 362.00, showing a lower variability of 9.24%. The mean chlorophyll *a*/*b* ratio was 1.59, the median was 1.61, the minimum was 1.14, and the maximum was 1.94, with a variation coefficient of 7.63% (Table 1).

The anthocyanin contents (AnC, nmol cm^{-2}) were 23.78, 23.59, 18.36, and 27.48, respectively, with a variation coefficient of 6.52%. The mean flavonoid content (Flv, nmol cm^{-2}) was 34.02, the median was 32.94, the minimum was 17.97, and the maximum was 51.74, with a coefficient of variation of 18.21%.

On a mass basis, chlorophyll *a* (mg g^{-1}) had a mean of 10.53, a median of 10.30, a minimum of 0.96, and a maximum of 17.50, showing high variability with a coefficient of 28.99%. Similarly, chlorophyll b (mg g^{-1}) exhibited high variability, with a mean of 6.64, a median of 6.85, a minimum of 0.64, and a maximum of 11.77, with a coefficient of variation of 29.01%. The mean total chlorophyll *a*+*b* concentration (Chl*a*+*b*, mg g^{-1}) was 17.16, the median was 17.46, the minimum was 1.60, and the maximum was 27.88, with a variation of 28.68%. On a mass basis (Car, mg g^{-1}), the mean carotenoid content was 3.64, the median was 3.57, the minimum was 0.33, and the maximum was 6.40, with a high coefficient of variation of 29.58%.

The mean anthocyanin content (AnC, µmol g^{-1}) was 3.37, with a median of 2.92, a minimum of 0.24, and a maximum of 5.75, with a variability of 37.07%. The mean flavonoid content (Flv, µmol g^{-1}) was 4.94, with a median of 3.75, a minimum of 0.33, and a maximum of 11.32, with the highest coefficient of variation at 46.51%. The mean phenolic compound content (Phe, mL L^{-1}) was 57.91, the median was 57.59, the minimum was 29.02, and the maximum was 111.31, with a coefficient of variation of 29.66%.

The mean DPPH radical scavenging activity was 91.73, with a median of 91.68, a minimum of 88.58, and a maximum of 99.30, indicating minimal variability with a coefficient of variation of 1.35%. Lignin (mg g^{-1}) had a mean of 307.67%, a median of 303.22%, a minimum of 178.09%, and a maximum of 422.13%, with a coefficient of variation of 19.68%. Finally, cellulose (nmol mg^{-1}) displayed a mean of 725.52, a median of 671.16, a minimum of 322.95, and a maximum of 1386.90, showing significant variability with a coefficient of variation of 37.39% (Table 1).

3.2. Chlorophyll a Fluorescence Kinetics

The two Tradescantia species displayed different chlorophyll a fluorescence kinetics in their leaves (Figure 2). The OJIP curves follow the names of the distinct phases O (origin), L, K, J, I, and P (peak), which are essential for calculating the JIP test parameters based on a logarithmic scale.

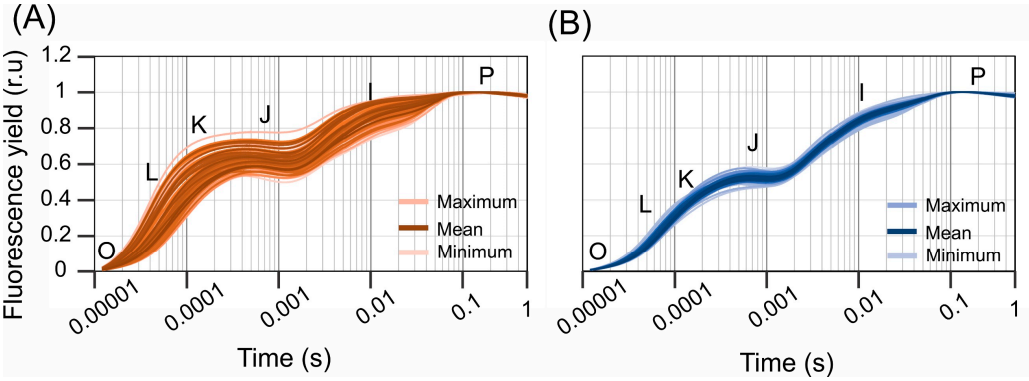

Figure 2. Spectral chlorophyll a fluorescence kinetics in leaves. (**A**) *Tradescantia spathacea* (L.) Olof Swartz. (**B**) *Tradescantia pallida* (Rose) DR. Hunt., species. The O, L, K, J, I, and P phases are based on a logarithmic scale (Time, s). (n = 100).

The OJIP curves indicated significant differences in pigments between the two species ($p < 0.01$), as measured by the photosynthetic performance. Significant reductions in variable fluorescence were observed at key points of 20 µs (ΔL), 300 µs (ΔK), 2 ms (ΔJ), 10 ms (ΔI), and 40 ms (ΔP). The curves illustrate different patterns of chlorophyll a fluorescence kinetics between *Tradescantia spathacea* and *Tradescantia pallida* plants (Figure 2A,B).

Further analysis revealed that points O and P had almost the same chlorophyll a fluorescence intensity, based on fluorescence yield for both species. However, *Tradescantia pallida* consistently showed greater fluorescence at points L, K, J, and I than *T. spathacea*, indicating possible differences in photosynthetic apparatus efficiency.

3.3. Hyperspectral Reflectance, Transmittance, and Absorbance Curves

There were noticeable differences in the reflectance between *Tradescantia spathacea* and *Tradescantia pallida* at specific wavelengths within each spectral range (Figure 3A,B). In the VIS spectrum (400–700 nm), a significant difference was observed at 544 nm. The largest difference in the NIR range (700–1300 nm) was observed at 700 nm. For the SWIR1 spectrum (1300–1800 nm), the most evident contrast was observed at 1441 nm, and in the SWIR2 range (1800–2500 nm), the most marked change was observed at 2488 nm. The consistently low p-values ($p < 0.01$) highlight the statistical importance of these results, implying that these wavelengths are essential for separating the two *Tradescantia* species based on their reflectance.

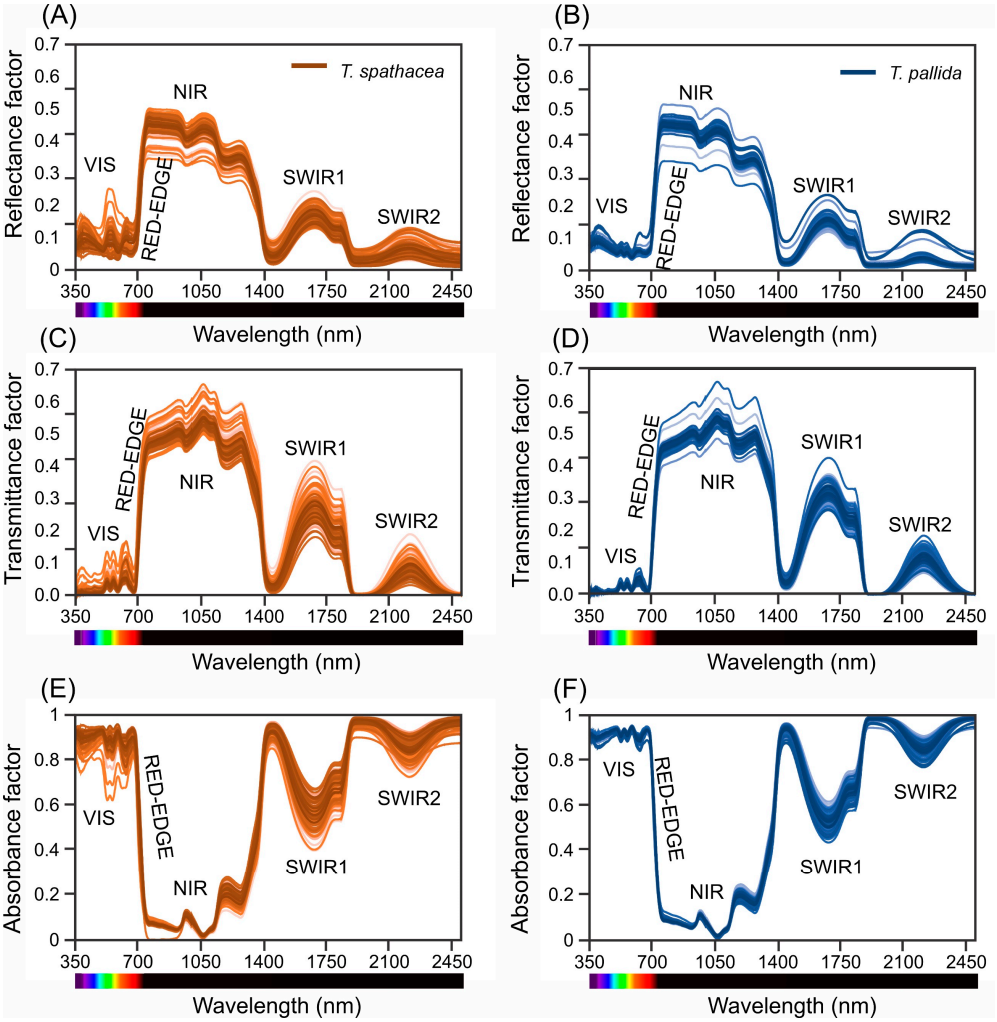

Figure 3. Spectral leaf reflectance, transmittance, and absorbance curves from 350 to 2500 nm for *Tradescantia spathacea* (L.) Olof Swartz and *Tradescantia pallida* (Rose) D.R. Hunt., species. (**A**,**B**) Reflectance curves. (**C**,**D**) Transmittance curves. (**E**,**F**) Absorbance curves. For clarity, *Tradescantia spathacea* is represented by orange lines, while *Tradescantia pallida* is indicated by blue lines ($n = 100$).

The transmittance values also showed substantial differences between the species at certain wavelengths within each spectral band (Figure 3C,D). In the VIS spectrum, the largest difference was observed at 400 nm. The peak difference within the NIR spectrum was at 1125 nm, whereas in the SWIR1 spectrum, it was at 1607 nm, and the SWIR2 spectrum peaked at 2175 nm. These significantly low *p*-values indicate that transmittance at these selected wavelengths can be used to distinguish *Tradescantia spathacea* from *Tradescantia pallida* species.

In the absorbance analysis, significant differences were detected at specific wavelengths across spectral bands (Figure 3E,F). The most notable changes were observed at 495 nm within VIS-Blue, 498 nm in VIS-Blue-Green, 733 nm in VIS-Red-Far-Red, 800 nm in NIR-Far-Red, 1117 nm in the NIR, 1575 nm in SWIR1, and 2175 nm in SWIR2. The extremely low p-values associated with these wavelengths verify their statistical significance and suggest that absorbance at these wavelengths is crucial for distinguishing *Tradescantia spathacea* from *Tradescantia pallida* species (Figure 3).

3.4. Principal Component Analysis for Fluorescence, Reflectance, Transmittance, and Absorbance Sensors

Figure 4 shows a principal component analysis (PCA) that reveals the spectral differences in the leaves of *Tradescantia spathacea* and *Tradescantia pallida* using various sensors for fluorescence, reflectance, transmittance, and absorbance (Figure 4A–D).

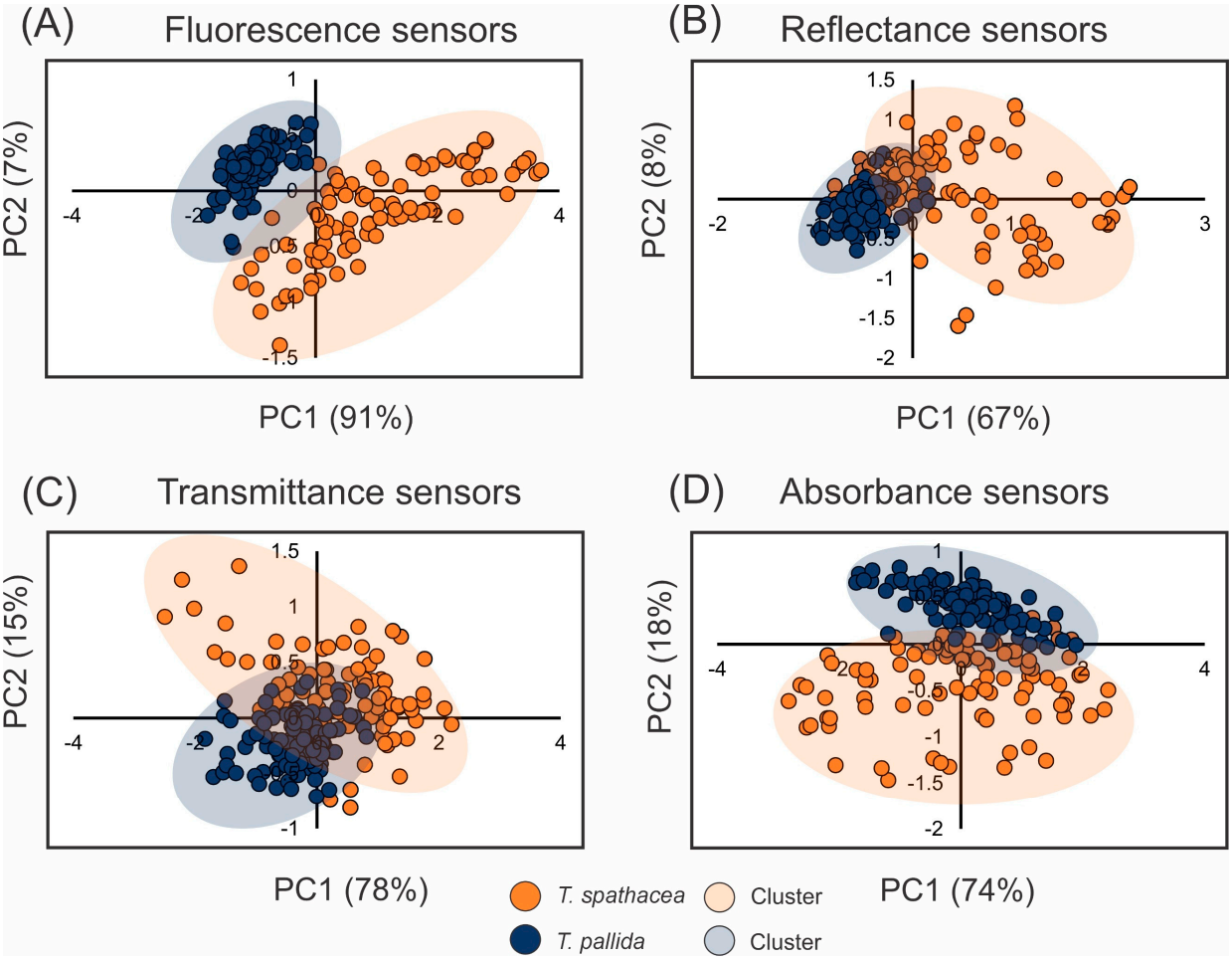

Figure 4. Principal component (PC) from 350 to 2500 nm in the leaves of *Tradescantia spathacea* (L.) Olof Swartz and *Tradescantia pallida* (Rose) D.R. Hunt., plants. (**A**) Fluorescence sensors. (**B**) Hyperspectral reflectance sensors. (**C**) Hyperspectral transmittance sensors. (**D**) Hyperspectral absorbance sensors. Clustering-coloured leaves are displayed as orange (*T. spathacea*) and blue (*T. pallida*) circles (n = 100).

Figure 4A shows the PCA for the fluorescence sensors, where *Tradescantia spathacea* is in orange and *Tradescantia pallida* is shown in blue. There was a clear separation along Principal Component 1 (PC1), which accounted for 91% of the variance, highlighting distinct fluorescence patterns for each species.

Figure 4B shows the PCA of the reflectance sensors. Here, a moderate difference was observed in PC1, which accounted for 67% of the total variance, indicating different reflectance features between the two species.

Figure 4C shows the PCA for transmittance sensors, showing a noticeable distinction between *Tradescantia spathacea* and *Tradescantia pallida* along both PC1 and PC2, explaining 78% and 15% of the variance, respectively. This implies that there were significant species-specific transmittance signatures.

Figure 4D shows the PCA for the absorbance sensors, with PC1 explaining 74% of the variance and PC2 accounting for 18%. This separation suggests strong differences in absorbance between the species.

The shaded regions within each shape show clusters of data points, reflecting the diversity within each species and the level of resemblance between them. The PCA results demonstrated the value of these spectral measurements for distinguishing between the two species of Tradescantia.

By analysing Figure 5A–L, each of which shows the variability and loadings across different spectral measurements, one can delineate the principal component contributions to spectral data interpretation for fluorescence, reflectance, transmittance, and absorbance (Figure 5).

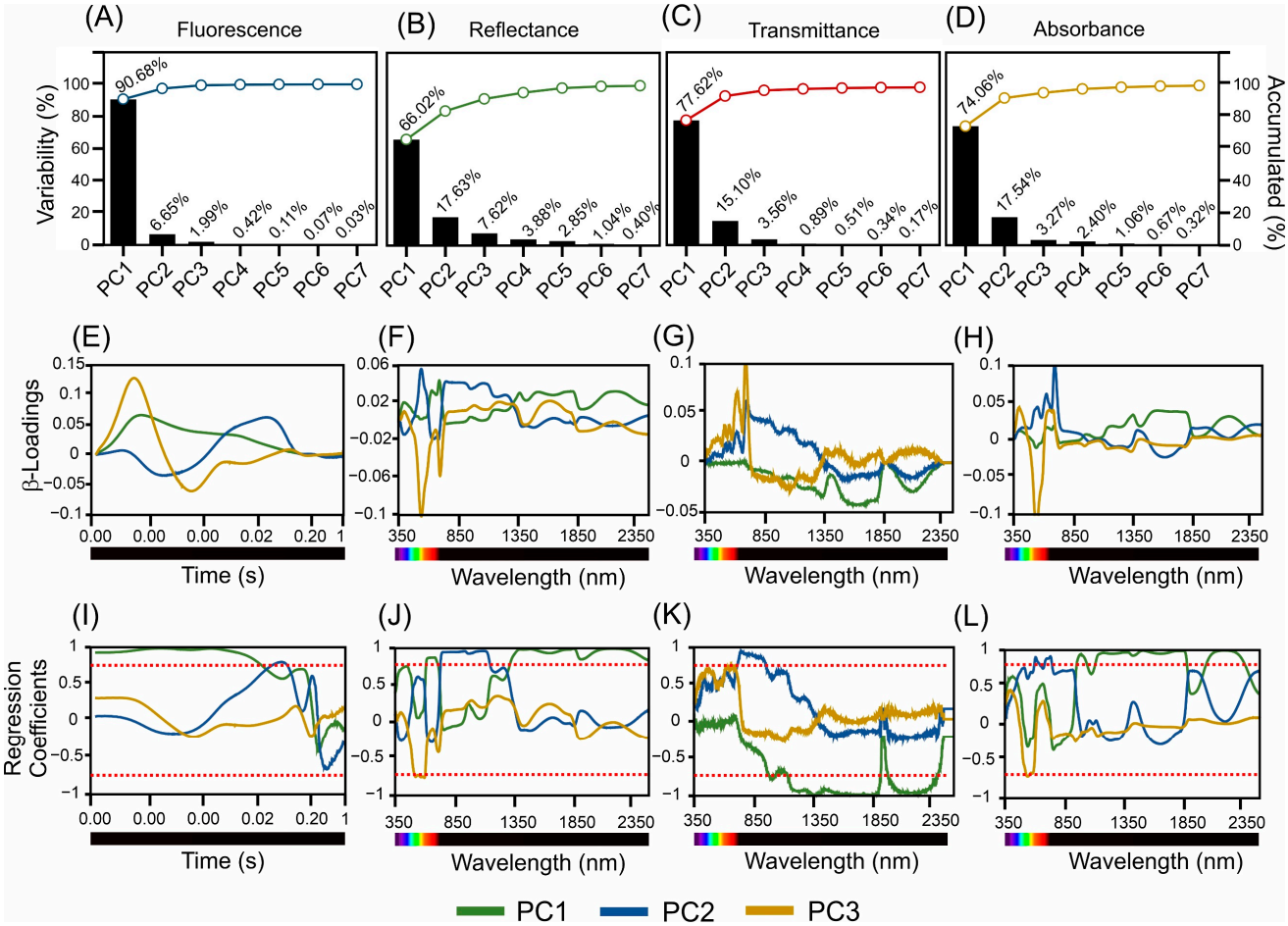

Figure 5. Displays scores, β-loadings, and regression coefficients obtained from fluorescence sensor, reflectance, transmittance, and absorbance hyperspectral analyses of *Tradescantia spathacea* (L.) Olof Swartz and *Tradescantia pallida* (Rose) D.R. Hunt. plants. (**A**–**D**) Variability and accumulation (%) based on three principal components. (**E**–**H**) β-Loading, corresponding to the sensors. (**I**–**L**) Regression coefficients for PC1-3 from 350 to 2500 nm. The green line represents PC1. The blue line represents PC2. The orange line represents PC3. The dashed red line delimits −0.75 to +0.75.

Figure 5A shows the variance captured by the principal components in the fluorescence data, with PC1 accounting for the majority of the variance (90.68%), followed by significantly smaller contributions from subsequent components. The reflectance data in Figure 5B show that PC1 was the dominant factor explaining 60.02% of the variability. The other components progressively contributed less, with PC2 and beyond explaining less than 20% of the variance. Figure 5C shows the transmittance data, with PC1 being pivotal and capturing 77.82% of the variance. PC2 also plays a more substantial role than the reflectance data, accounting for 15.10% of the variability. The absorbance variability in Figure 5D was primarily determined by PC1, which explained 74.06% of the total variance, followed by smaller yet significant contributions from PC2 and PC3.

Figure 5E–H presents the β-loadings across the time or wavelength range for each principal component, reflecting their weight in each spectral band. Figure 5I–L correlates these findings with the regression coefficients to indicate the influence of each wavelength on the respective spectral measurements. Figure 5F shows the leading wavelengths for PC1 located in the blue, green, red, NIR, SWIR1, and SWIR2 bands. The reflectance datasets for PC2 and PC3 also highlighted similar influential wavelengths, confirming their significance across the spectrum. Figure 5G shows the crucial wavelengths for the transmittance of PC1 in the blue and SWIR2 bands. The subsequent principal components, depicted in Figure 5J,K, corroborate the importance of these wavelengths, suggesting consistency in the influential spectral bands across different components.

The absorbance measurements in Figure 5H for PC1 show the selection of key wavelengths from the blue to the SWIR2 range. This is in line with the absorbance results for PC2 and PC3, as shown in Figure 5K,L, which further confirms the relevance of the wavelengths.

A comprehensive examination of these findings, in conjunction with the regression coefficients depicted in Figure 5I–L, provides a profound understanding of the most influential wavelengths across the reflectance, transmittance, and absorbance spectra. The variance explained by the principal components underscores the significant spectral regions that differentiate the studied variables (Figure 5A–L).

3.5. Hyperspectral Vegetation Index for Chlorophyll a Fluorescence, Reflectance, Transmittance, and Absorbance

Figure 6 shows a contour plot that maps the coefficient of determination (R^2) values from linear regression analyses, which evaluates the relationship between the levels of various biochemical compounds and chlorophyll fluorescence (ChlF) over a time logarithmic scale of 0.00001 to 1 s (Figure 6A–Q).

Figure 6A,B shows the R^2 values for chlorophyll *a* and chlorophyll *b*, respectively, measured in mg m^{-2}, over the time scale. Areas that changed from dark to light red indicate higher R^2 values, indicating stronger relationships at certain time points. In Figure 6C, the total chlorophyll (Chl*a*+*b*) content is plotted, showing the R^2 values over time, indicating the time points at which the fluorescence data best predicted the total chlorophyll content. Figure 6D–F show the contour maps for carotenoids, anthocyanins, and flavonoids, measured in mg m^{-2} and nmol cm^{-2}, respectively. These plots show the temporal patterns of the correlation between chlorophyll fluorescence and the levels of these compounds.

Figure 6G–I focus on the chlorophyll *a*/*b* ratio, chlorophyll *a*, and chlorophyll *b* on a mass basis (mg g^{-1}). The plots show different correlations, with some timeframes showing higher R^2 values. Figure 6J,K,L shows the total chlorophyll (Chl*a*+*b*), carotenoids, and anthocyanins per mass, highlighting the times when fluorescence is most indicative of the presence of these compounds. In Figure 6M,N, the maps for flavonoids and phenolic compounds, measured in µmol g^{-1} and mL L^{-1}, respectively, show areas of stronger and weaker correlations over the fluorescence time scale. Figure 6O shows the R^2 values for the DPPH assay, which is a measure of antioxidant activity, showing less variation over time.

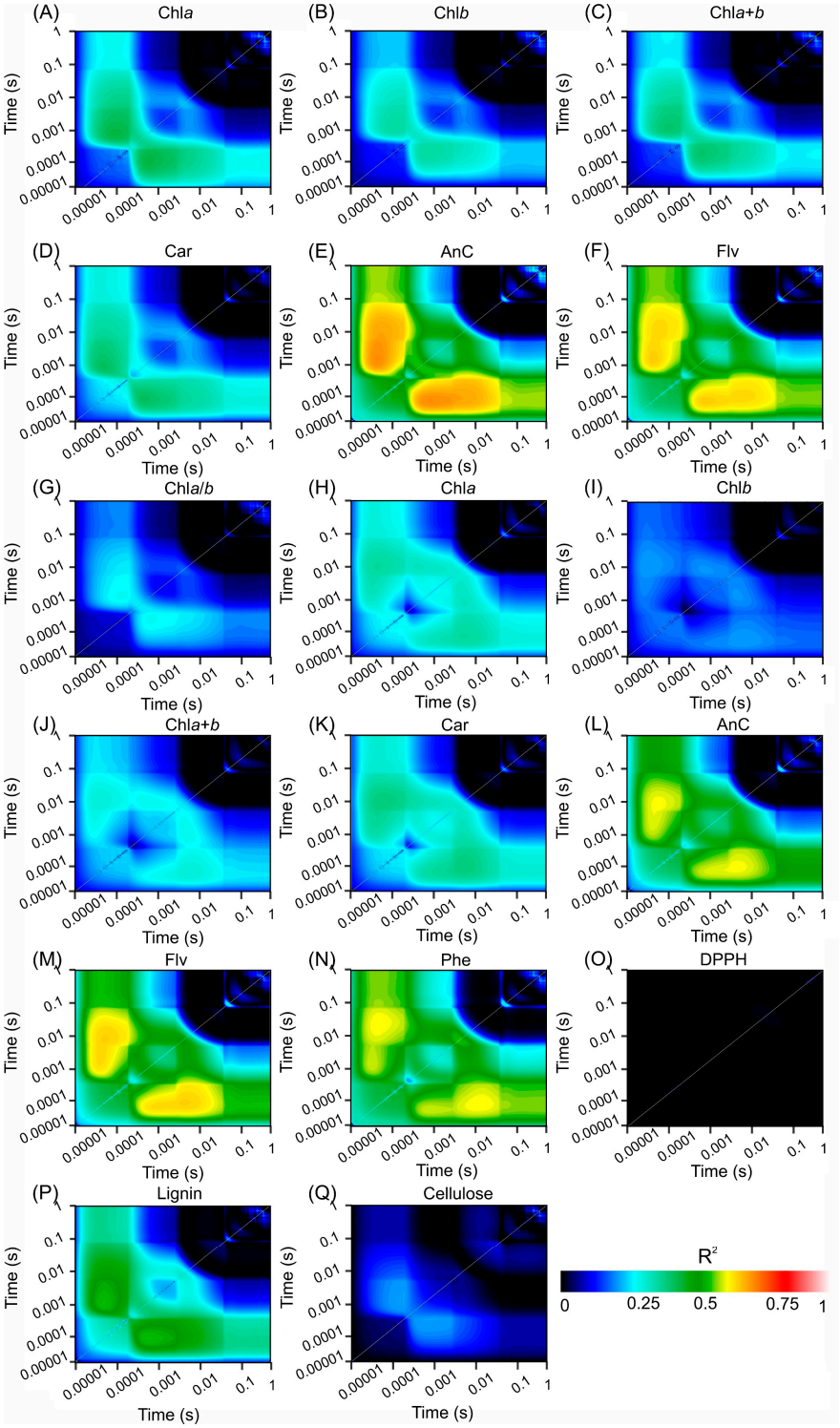

Figure 6. Count plot map of the coefficient of correlation (R^2) from the linear regression between the concentration of compounds and wavelength1 vs. wavelength2 from ChlF from 0.00001 to 1 s. (**A**) Chlorophyll *a* (mg m^{-2}). (**B**) Chlorophyll *b* (mg m^{-2}). (**C**) Total chlorophyll (*a*+*b*) (mg m^{-2}). (**D**) Carotenoids (mg m^{-2}). (**E**) Anthocyanins (nmol cm^{-2}). (**F**) Flavonoids (nmol cm^{-2}). (**G**) Chl *a*/*b* ratio. (**H**) Chlorophyll *a* (mg g^{-1}). (**I**) Chlorophyll *b* (mg g^{-1}). (**J**) Total chlorophyll (*a*+*b*) (mg g^{-1}). (**K**) carotenoids (mg g^{-1}). (**L**) Anthocyanins (µmol g^{-1}). (**M**) Flavonoids (µmol g^{-1}). (**N**) Phenolic compounds (mL L^{-1}). (**O**) DPPH. (**P**) Lignin (mg g^{-1}). (**Q**) Cellulose (nmol mg^{-1}). Dark blue to light red indicate increased associations. (n = 200).

Figure 6P,Q shows the lignin and cellulose contents, measured in mg g^{-1} and nmol mg^{-1}, respectively. This figure shows specific time intervals with strong relationships between fluorescence and compound levels.

Overall, these contour maps provide a visual representation of the temporal and quantitative relationships between chlorophyll fluorescence dynamics and the levels of various biochemical compounds in plant leaves. The gradation from dark to light red areas shows where the relationship is strongest, offering valuable insights into the moments when ChlF is the most informative of the compound levels.

Figure S1 shows a series of contour plots that illustrate the strength of the correlation, as indicated by the coefficient of determination (R^2), across two wavelengths (wavelength1 and wavelength2) for various biochemical compounds using hyperspectral reflectance data (Figure S1A–Q).

Figure S1A–C displays the relationships for chlorophyll *a*, chlorophyll *b*, and total chlorophyll (Chl*a*+*b*), respectively, measured in mg m^{-2}. Areas with higher R^2 values, which changed from dark blue to red, showed stronger correlations, especially for specific wavelength pairings. In Figure S1D, the R^2 values for the carotenoids (mg m^{-2}) are plotted, showing regions where the correlation between the reflectance at certain wavelengths and the carotenoid concentration is more evident. Figure S1E,F, which represents anthocyanins (nmol cm^{-2}) and flavonoids (nmol cm^{-2}), respectively, reveals the spectral zones in which the reflectance data have greater explanatory power for the concentrations of these compounds. The chlorophyll *a*/*b* ratio is shown in Figure S1G, with regions of stronger association indicating wavelengths that are more closely related to this particular ratio.

For chlorophyll *a*+*b*, on a mass basis (mg g^{-1}), Figure S1H,I illustrates how some wavelength combinations correlated more strongly with their concentrations. Figure S1J–L presents the R^2 values for total chlorophyll (Chl*a*+*b*), carotenoids, and anthocyanins per mass of plant material, showing key wavelengths where reflectance data correlated strongly with compound concentrations. For flavonoids (μmol g^{-1}) and phenolic compounds (mL L^{-1}), Figure S1M,N reveals significant spectral areas where the correlations between reflectance and concentration are strongest. Figure S1O, which shows DPPH, an antioxidant activity marker, showed a nearly uniform correlation across all wavelength pairs, indicating a less clear relationship in the reflectance data. Finally, Figure S1P,Q shows the correlation between lignin (mg g^{-1}) and cellulose (nmol mg^{-1}). Here, the selected wavelength pairings were shown to have a stronger association with the concentrations of these structural compounds.

Together, these contour plots reveal the complex relationships between reflectance at various wavelengths and the concentrations of different biochemical compounds, highlighting the possibility of using hyperspectral reflectance data to estimate compound concentrations in plant leaves. The change in colour from dark blue to red in the plots indicates the range of correlation strengths, with warmer colours indicating areas of greater predictive accuracy (Figure S1A–Q).

Figure S2 shows the correlations between different wavelengths of light passing through the plant tissues and their biochemical compounds. The R^2 values in the figure show which wavelengths of light are most related to the compound levels in plants.

Chlorophyll *a* and *b*, as shown in Figure S2A,B, had strong correlations with some visible and NIR wavelengths, especially when they interacted with specific NIR bands. Figure S2C shows that the transition from red to NIR light is highly predictive of the total chlorophyll (Chl*a*+*b*) content. As shown in Figure S2D, there were strong correlations between the levels of carotenoids at the edge of the visible and NIR light, indicating that these wavelengths affect carotenoid levels. The anthocyanin and flavonoid concentrations in Figure S2E,F exhibited sharp peaks and many correlations across different wavelengths, indicating that their spectral reflectance varied between species.

Figure S2G shows that some wavelengths were strongly related to the Chl *a*/*b* ratio, as indicated by the high R^2 values. Likewise, the chlorophyll *a* and *b* per mass in Figure S2H,I and the total chlorophyll (Chl*a*+*b*) per gram in Figure S2J had areas of high R^2 values, showing the wavelengths that tell us a lot about these chlorophyll levels.

The carotenoid and anthocyanin contents per mass, as shown in Figure S2K,L, exhibit a mixed pattern with strong hotspots, revealing the wavelengths that strongly reflect these compounds. Figure S2M,N, which shows flavonoids and phenolic compounds per gram, respectively, has high correlations in some spectral areas, revealing the regions that are most predictive of these compounds.

In contrast, the DPPH assay results in Figure S2O show no strong linear relationship between the wavelength and antioxidant activity, as seen in the even plot (Figure S2, see scale). Figure S2P,Q shows that lignin and cellulose have relatively high correlation values. These regions have wavelengths that are good indicators of the levels of these structural compounds.

Together, these findings demonstrate the complex links between spectral transmittance and biochemical compounds, providing a spectral signature that can be used to analyse plant constituents without destroying them. The colours in each plot show the strength of these links, with warmer colours showing regions of higher accuracy in the hyperspectral transmittance data (Figure S2A–Q).

Figure S3 shows how the absorbance data reveal how wavelengths and plant biochemical compounds interact according to their concentrations. Peaks with high correlations appear clearly in some spectral zones, showing that the absorbance at one wavelength is most useful for predicting the compound concentration when combined with another wavelength.

The chlorophyll *a* and *b* concentrations were highly correlated in the near-infrared region at approximately 700 nm. This trend is also true for the total chlorophyll content (Chl*a*+*b*), where wavelengths near 700 nm and shortwave infrared regions are strongly related to the chlorophyll content. The chlorophyll *a*/*b* ratio showed a similar correlation pattern, especially within the near-infrared range (Figure S3).

Carotenoid levels have noticeable correlations, especially within the overlap of the visible light range and the lower part of the near-infrared spectrum. Anthocyanin concentrations show a different pattern, with the highest correlations occurring over a wider range of wavelengths, indicating that multiple factors are involved in predicting anthocyanin levels through absorbance.

Flavonoid concentrations, shown in their contour plot, also had areas of high correlation, particularly in the interactions that occurred from the visible light range to the near-infrared spectrum. This finding implies a consistent effect of these wavelengths on the prediction of the flavonoid content (Figure S3).

The plots of structural compounds, such as lignin and cellulose, revealed that the concentrations of some wavelength combinations, especially those that cross from the near-infrared region to the shortwave infrared region, are somewhat related to their concentrations. In these contour plots, a range of correlations was observed, with the colour intensity representing the minor of the relationship. The gradients in these plots helped us identify the wavelength interactions that were most predictive of the concentrations of these important plant compounds (Figure S3A–Q).

3.6. Parameters Predicted by Biochemical Compounds

3.6.1. Calibration and Validation Models

Table S1 shows the statistical metrics from the PLSR models for different modalities in the comprehensive evaluation of spectrometric methods for estimating biochemical pigment parameters. The aim of this PLSR model was to compare the calibration and cross-validation results of chlorophyll and carotenoid predictions using fluorescence, reflectance, transmittance, and absorbance measurements in *Tradescantia* species (Table S1).

The fluorescence sensor calibration for chlorophyll a had an R^2 of 0.56, with a small decrease to 0.55 in cross-validation and corresponding RPDs of 1.21 and 1.19, indicating moderate model strength. Carotenoid predictions under fluorescence showed higher calibration accuracy, with an R^2 of 0.64 and an RPD of 1.31, which slightly decreased to an R^2 of 0.61 and an RPD of 1.26 in cross-validation, suggesting a more reliable model.

The reflectance measurements displayed similar trends, with chlorophyll a having an R^2 of 0.58 in calibration and 0.53 in cross-validation and carotenoids having R^2 values of 0.61 and 0.56, respectively, implying consistent performance but with some room for improvement in cross-validation. Transmittance was highly effective, especially for carotenoids, which showed an impressive calibration R^2 of 0.84. However, the cross-validation phase indicated a reduction in the predictive accuracy, with an R^2 of 0.59. The absorbance data for chlorophyll a showed a strong calibration R^2 value of 0.61, with a slight decrease to 0.56 in cross-validation. The carotenoids measured via absorbance had high calibration and cross-validation R^2 values of 0.64 and 0.59, confirming the effectiveness of this modality in evaluating pigment concentration (Table S1).

Statistical parameters such as slope, offset, RMSE, RPD, and bias present across these sensors provide a detailed understanding of each model's predictive power and potential limitations. Notably, anthocyanin concentration predictions stand out with an R^2 reaching up to 0.92 in calibration and maintained in cross-validation for the fluorescence sensor, highlighting the high quality of this modality for this specific pigment.

Overall, the data presented offer a thorough quantitative analysis of spectrometric techniques for the non-destructive estimation of biochemical compounds (Table S1).

3.6.2. Predicted

Table S2 shows the predictive performance of PLSR across different spectroscopic methods for estimating biochemical compound concentrations in the Tradescantia species. The table benchmarks performance metrics comprising the correlation coefficient (r), R-square for model fit (R^2), slope, offset, SEP, RMSEP, RPD, and bias, offering a precision selection for each sensor.

Fluorescence-based predictions revealed moderate predictability for chlorophyll *a*, with an R^2 value of 0.20. Carotenoids had limited accuracy, as indicated by an R^2 value of 0.13. Conversely, anthocyanins demonstrated a higher model fit, with an R^2 value of 0.42, suggesting enhanced predictability with this sensor.

Reflectance-based assessments delivered slightly superior R^2 values for chlorophyll *a* (Chl*a*) and carotenoids of 0.26 and 0.16, respectively, indicating moderate precision. Anthocyanins outperformed the other tested compounds, with an R^2 value of 0.52, indicating increased reliability. Transmittance measurements yielded analogous R^2 values for chlorophyll *a* and carotenoids of 0.23 and 0.10, respectively, highlighting the predictive limitations of this technique for these compounds. However, anthocyanins exhibited robust predictability with an R^2 of 0.52, mirroring the reflectance findings.

The absorbance modality improved the R^2 values for chlorophyll *a* and carotenoids to 0.24 and 0.12, respectively. The R^2 of 0.53 for anthocyanins confirmed the sensor's ability to predict these biochemical compounds. The RMSEP and RPD values across all sensors demonstrated variable precision and reliability, with higher RPD values indicating superior predictive capabilities, particularly for anthocyanins in most spectroscopic modalities. Bias values pinpointed the deviations from an ideal zero, accentuating opportunities for model refinement.

Further detailed examination of the specific compounds using the maximum factors in PLS revealed varying degrees of predictability. For example, phenolics (Phe) exhibited an R^2 of 0.53 with a PLS factor of 7, denoting a moderately strong fit, whereas lignin with the same factor showed a weak fit with an R^2 of 0.02. The anthocyanin content, as predicted by PLS with a factor of 5, showed a strong R^2 of 0.42 and an RPD of 1.31, indicating the reliability of the model.

A comparison of the predicted and observed values in four different scatter plots showed that absorbance was the most consistent method, with better correlations for some parameters than for chlorophyll fluorescence, reflectance, transmittance, and absorbance data. As shown in Figure 7, for chlorophyll a fluorescence, the R^2 values for chlorophyll *a* (Chl*a*)area and mass were moderate, indicating some correlation but with variability. The carotenoid area had a weak prediction, as shown by the low R^2 value, and this pattern continued for the Chl*a*/*b* ratio. However, flavonoid and anthocyanin mass measurements had higher predictability with relatively high R^2 values.

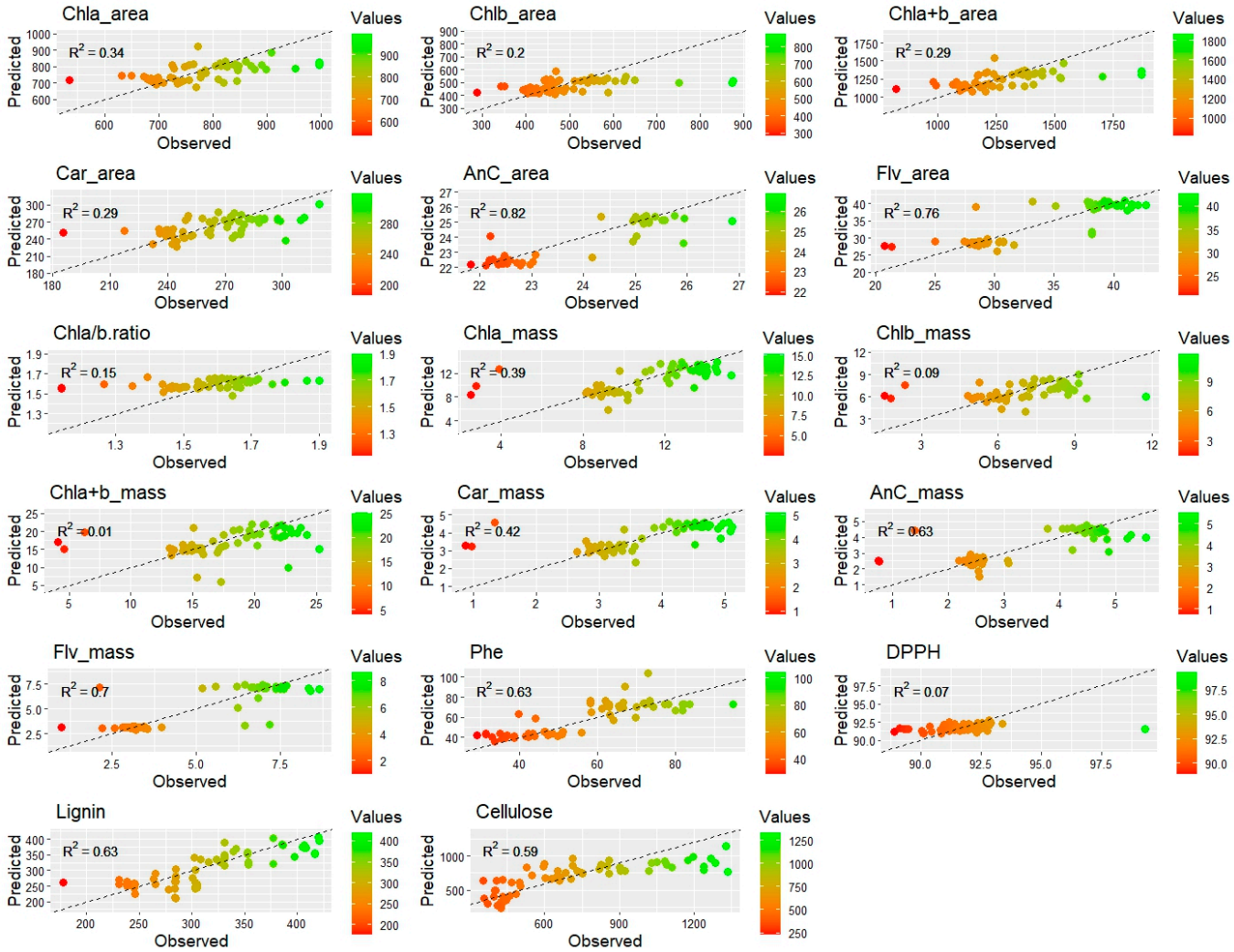

Figure 7. Observed vs. predicted data estimated by partial least squares regression (PLSR) with hyperspectral ChlF data. The R^2 value was adjusted using a linear equation. The red to green dots represent increased values, and the black dashed lines represent regression and 1:1 ratios, respectively. (n = 50).

As shown in Figure S4, the reflectance data were fairly consistent for the chlorophyll *a* area, with moderate R^2 values. Carotenoid area and anthocyanin mass also had reasonable predictive abilities. The reflectance was especially strong in predicting the flavonoid area and phenolic content, as shown by the higher R^2 values. However, the Chl*a*/*b* ratio and cellulose content were less reliably predicted by the reflectance, with lower R^2 values (Figure S4).

As shown in Figure S5, the overall transmittance data exhibited weaker correlations. However, anthocyanin mass predictions were much more accurate, unlike the Chl*a*/*b* ratio, which remained poorly predicted across all the sensors. The flavonoid mass maintained a strong relationship with the observed transmittance, similar to its effect on the reflectance. The lignin content had moderate predictability with respect to the transmittance (Figure S5).

Finally, the absorbance data in Figure S6 correlated moderately with the observed values for the chlorophyll *a* (Chl*a*)-based area, with slight improvements in the ability of the other methods to predict the carotenoid content. The anthocyanin mass predictions remained strong, and the trend of weak predictability for the Chl*a*/*b* ratio continued. The flavonoid mass showed a good correlation, although it was slightly lower than that of the transmittance data. The predictions for lignin and cellulose content by absorbance were moderate but improved compared to those for reflectance and transmittance (Figure S6).

The plots had greater green colour intensity, especially in the absorbance data, showing stronger correlations for specific parameters, suggesting that absorbance could be a more reliable predictor of biochemical content (Figures S4–S6).

4. Discussion

The combination of hyperspectral sensors in our study has proven to be highly effective in advancing the predictive capabilities of remote sensing and aligns with plant physiological research (Figures 1–7 and S1–S6). These sensors not only capture a wide spectrum of data but also facilitate a deeper understanding of biochemical and biophysical compound predictions that align physiological processes, revealing more than what meets the eye at the superficial level. By integrating hyperspectral vegetation indices (HVIs) with other analytical tools, we have deepened our analysis and demonstrated significant improvements in monitoring and predicting plant health and better understanding fingerprints that use different sensors for analyses.

This enhanced approach allowed us to construct a detailed spectrum of plant responses to pigments and structural compounds, which was corroborated by our findings that showed a positive impact on the accuracy of chlorophyll a fluorescence predictions following [22,48,49]. The integration of various sensor technologies in our research established a robust framework for conducting nuanced and comprehensive plant analyses, effectively extending the capabilities of traditional methods and providing new insights into remote sensing for environmental and agricultural analyses [2,26,50].

Our results underscore the benefits of sensor integration, validating the approach as a transformative step in the field of precision agriculture and improving environmental monitoring. This is a promising direction for future research, potentially leading to more refined strategies with SFI or non-imaging for crop management and ecological assessments [27,51–53].

The application of hyperspectral sensors in predicting chlorophyll a fluorescence parameters has recently gained considerable attention in remote-sensing research [22,26,27,39,40]. The interactions between light and plant tissues, including absorption, reflection, and transmission, provide valuable insights beyond the more accurate prediction of compounds in relation to integrated sphering or methods for analysing single sensors. They reveal crucial physiological processes and adaptive mechanisms.

Hyperspectral vegetation indices (HVIs) are powerful tools in precision agriculture because of their ability to measure a wide range of physiological, biochemical, and structural parameters in leaves of different thicknesses [18,22,54,55]. These indices enable the discrimination and monitoring of different environmental stresses, such as water and nitrogen deficiency, by analysing the spectral reflectance patterns of crops or studies on different plants [6,14,36,56,57].

For instance, certain narrow-band HVIs are particularly sensitive to changes in water and nitrogen levels, allowing for a nuanced assessment of crop responses under varying conditions of irrigation and fertilisation. The DATT index and HVI, which focus on near-infrared and red-edge wavelengths, have shown efficacy in correlating with chlorophyll

content, whereas indices such as the double difference index (DD) are highly correlated with leaf gas exchange, highlighting their potential for identifying and differentiating between water and nitrogen stress levels in crops [20,25,38,58,59].

Moreover, HVIs can integrate data from chlorophyll fluorescence and hyperspectral measurements, providing a comprehensive map that identifies regions with specific biochemical and biophysical attributes. This integration is crucial for generating accurate maps that guide agricultural interventions, optimise resource use, and improve crop management strategies.

4.1. Hyperspectral and Principal Component Analysis by Reflectance, Transmittance, and Absorbance

Hyperspectral sensors provide detailed, in-depth spectral data, enabling the comprehensive analysis of plant biochemical and biophysical characteristics [23,60]. Reflectance data offer insights into the surface and internal structures of leaves, indicating variations in chlorophyll concentrations and potential cellular modifications. This finding aligns with previous research that demonstrated how changes in reflectance can signify physiological changes within plant tissues [7,27]. Similarly, transmittance data are critical for understanding how light diffuses within a leaf, thereby providing additional data points that enhance our understanding of leaf structure and function [61,62].

However, hyperspectral datasets require sophisticated data-reduction techniques, such as principal component analysis (PCA). In this study, PCA was effectively utilised to identify critical spectral regions that correlate with variations in chlorophyll a fluorescence, which is crucial for developing robust remote-sensing applications [59,63]. This precise identification significantly enhances the accuracy of the remote-sensing tools. Additionally, the predictive capabilities of these hyperspectral measurements were rigorously evaluated, focusing on the coefficients of variation and range of values obtained to ensure data reliability across a broad electromagnetic spectrum [15,64]. Our findings demonstrate that when these advanced passive sensor techniques are applied correctly, they provide detailed insights into plant health and photosynthetic performance, which are crucial for accurate plant phenotyping and health monitoring, as well as available fingerprints in leaves with different pigments and depths.

Finally, the integration of different sensor types, both hyperspectral and chlorophyll fluorescence, was explored to enhance the predictive modelling capabilities. This synergy allows broader application of the data, enhancing the ability to effectively predict and monitor various plant health parameters. This comprehensive approach underscores the potential of hyperspectral non-imaging to revolutionise plant physiological research and agricultural practices by providing a deeper understanding of plant dynamics at the molecular level with fast and accurate methods.

4.2. Predictive Modelling-Based Reflectance, Transmittance, and Absorbance

The fusion of hyperspectral data and partial least squares (PLS) modelling has emerged as a revolutionary approach in plant science, significantly enhancing our ability to predict and understand complex physiological traits [23,58,65,66]. The integration of reflectance, transmittance, and absorbance measurements with advanced multivariate algorithms, such as PLS, not only substantiates the vital role of these parameters as indicators of photosynthetic performance and the functionality of the electron transport chain but also boosts the precision of our predictive models.

Variable importance in projection (VIP) scores and hyperspectral vegetation indices (HVIs) are tools for isolating the most informative wavelengths from hyperspectral datasets, refining the predictive accuracy of models, and enabling a more detailed understanding of plant characteristics [22,23,67]. Such methodologies underscore the utility of identifying spectral regions that are rich in information and are directly related to the physiological state of plants [27,64,68,69].

The use of principal component analysis (PCA) to handle a substantial amount of large-scale hyperspectral data simplifies the complexity by identifying primary spectral regions indicative of changes in chlorophyll a fluorescence parameters. These spectral signatures are essential for crafting remote-sensing tools that can noninvasively assess plant properties, such as chlorophyll and potassium and nitrogen content [38,50].

The predictive models developed from this integrated approach support real-time with high-speed fluorescence lifetime imaging for analysis with a microscope and non-imaging spectroradiometer methods reinforce the power of remote sensing in broad-scale monitoring, conforming to contemporary perspectives that acknowledge the transformative potential of these technologies for global monitoring and productivity management. Real-time monitoring is pivotal for informed decision-making in agriculture, forestry, and other remote-sensing-dependent sectors, leading to enhanced productivity and sustainability [28,29]. In future applications, compressed FLIM has a striking advantage in acquiring a widefield lifetime image within a single camera snapshot. This eliminates motion artifacts and enables fast recording of biological events. There is also the possibility of associating other sensors for remote sensing [70].

However, it is essential to recognise that while our study has made significant strides in the application of hyperspectral and PLS models, further research is needed to extend these techniques to various plant species and environmental conditions.

Whole-spectrum models, such as PLSR, LDA, and SVR, have shown exceptional efficacy in classifying and predicting leaf properties, offering invaluable insights for interpreting chlorophyll a fluorescence data that are critical for JIP-test evaluations [30,58,71,72]. By leveraging the full spectrum of available data, these models ensure a comprehensive analysis of intricate leaf attributes, including the interactions between leaf optical properties and the complex chemistry of molecules in variegated leaves.

The combination of hyperspectral sensors and chlorophyll a fluorescence has proven to be highly effective in predicting biochemical compounds in Tradescantia leaves. Our findings, which align with other studies and perspectives, demonstrate the consistent effects of spectral resolution (SR) and sensor altitude on the accuracy of solar-induced fluorescence (SIF) quantification. In contrast to sub-nanometre sensors, which are precise but costly and difficult to operate, narrow-band sensors are more accessible and can be installed on drones and lightweight aircraft. We suggest that future studies utilise a combination of sensors, particularly when analysing plants and leaves with multiple overlapping pigments, to evaluate the efficiency of narrow-band sensors in producing SIF760 estimates. Furthermore, the incorporation of machine learning, deep learning, and other hyperspectral vegetation indices could significantly enhance these analyses.

5. Conclusions

This study has shown the comprehensive ability of hyperspectral remote sensing to estimate biochemical and structural compounds in Tradescantia species by utilising the intricate synergy between chlorophyll fluorescence, reflectance, transmittance, and absorbance measurements. The accuracy of the multivariate statistical models validates the effectiveness of these methods in remote-sensing applications, and the identified spectral regions, spanning from blue to shortwave infrared, were confirmed to be critical for the non-destructive evaluation of plant physiological status.

The strategic application of hyperspectral vegetation indices (HVIs) in selecting informative wavelengths has notably refined the results of partial least squares (PLS) regression models. The precision of these models attests to the significant role of hyperspectral sensors in the remote assessment of plant photosynthesis and health.

For broader remote sensing, the findings of this study can serve as a benchmark for the potential of also applying other passive sensors and hyperspectral imaging in diverse plant studies. Future research should extend these approaches to a larger variety of species and incorporate them into different field conditions. Such expansions could enhance the accuracy and generalisability of the models, as well as other methods that align

with hyperspectral sensors, as tools in the fields of plant remote sensing and agricultural monitoring of variegatum leaves.

Supplementary Materials: The following supporting information can be downloaded at: https://www.mdpi.com/article/10.3390/rs16111910/s1, Table S1. Statistical metrics from the PLSR model in the calibration and cross-validation phases. R-square for model goodness-of-fit (R^2), slope, offset, root mean squared error (RMSE), ratio of performance to deviation (RPD), and bias to base models (a prediction using an independent sample coupled to calibrated models), biochemical compound from ChlF (single sensor), reflectance (single sensor), transmittance (single sensor), and absorbance (two sensors) hyperspectral data of *Tradescantia spathacea* (L.) Olof Swartz and *Tradescantia pallida* (Rose) D.R. Hunt. plants. (n = 150); Table S2. Statistical metrics of the PLSR model in the predicted phases. R-square for model goodness-of-fit (R^2), slope, offset, root mean squared error (RMSE), ratio of performance to deviation (RPD), and bias to base models (a prediction using an independent sample coupled to calibrated models), biochemical compound from ChlF (single sensor), reflectance (single sensor), transmittance (single sensor), and absorbance (two sensors) hyperspectral data of *Tradescantia spathacea* (L.) Olof Swartz and *Tradescantia pallida* (Rose) D.R. Hunt. plants. (n = 50); Figure S1. Count plot map of the coefficient of correlation (R^2) from the linear regression between the concentration compounds and wavelength1 vs. wavelength2 from hyperspectral reflectance from 350 to 2500 nm. (A) Chlorophyll *a* (mg m^{-2}). (B) Chlorophyll *b* (mg m^{-2}). (C) Total chlorophyll (*a*+*b*) (mg m^{-2}). (D) Carotenoids (mg m^{-2}). (E) Anthocyanins (nmol cm^{-2}). (F) Flavonoids (nmol cm^{-2}). (G) Chl *a*/*b* ratio. (H) Chlorophyll *a* (mg g^{-1}). (I) Chlorophyll *b* (mg g^{-1}). (J) Total chlorophyll (*a*+*b*) (mg g^{-1}). (K) Carotenoids (mg g^{-1}). (L) Anthocyanins (µmol g^{-1}). (M) Flavonoids (µmol g^{-1}). (N) Phenolic compounds (mL L^{-1}). (O) DPPH. (P) Lignin (mg g^{-1}). (Q) Cellulose (nmol mg^{-1}). Dark blue to light red indicate increased associations. (n = 200); Figure S2. Count plot map of the coefficient of correlation (R^2) from the linear regression between the concentration compounds and wavelength1 vs. wavelength2 from hyperspectral transmittance from 350 to 2500 nm. (A) Chlorophyll *a* (mg m^{-2}). (B) Chlorophyll *b* (mg m^{-2}). (C) Total chlorophyll (*a*+*b*) (mg m^{-2}). (D) Carotenoids (mg m^{-2}). (E) Anthocyanins (nmol cm^{-2}). (F) Flavonoids (nmol cm^{-2}). (G) Chl *a*/*b* ratio. (H) Chlorophyll *a* (mg g^{-1}). (I) Chlorophyll *b* (mg g^{-1}). (J) Total chlorophyll (*a*+*b*) (mg g^{-1}). (K) and carotenoids (mg g^{-1}). (L) Anthocyanins (µmol g^{-1}). (M) Flavonoids (µmol g^{-1}). (N) Phenolic compounds (mL L^{-1}). (O) DPPH. (P) Lignin (mg g^{-1}). (Q) Cellulose (nmol mg^{-1}). Dark blue to light red indicate increased associations. (n = 200); Figure S3. Count plot map of the coefficient of correlation (R^2) from the linear regression between the concentration of compounds and wavelength1 vs. wavelength2 from the hyperspectral absorbance from 350 to 2500 nm. (A) Chlorophyll *a* (mg m^{-2}). (B) Chlorophyll *b* (mg m^{-2}). (C) Total chlorophyll (*a*+*b*) (mg m^{-2}). (D) Carotenoids (mg m^{-2}). (E) Anthocyanins (nmol cm^{-2}). (F) Flavonoids (nmol cm^{-2}). (G) Chl *a*/*b* ratio. (H) Chlorophyll *a* (mg g^{-1}). (I) Chlorophyll *b* (mg g^{-1}). (J) Total chlorophyll (*a*+*b*) (mg g^{-1}). (K) Carotenoids (mg g^{-1}). (L) Anthocyanins (µmol g^{-1}). (M) Flavonoids (µmol g^{-1}). (N) Phenolic compounds (mL L^{-1}). (O) DPPH. (P) Lignin (mg g^{-1}). (Q) Cellulose (nmol mg^{-1}). Dark blue to light red indicate increased associations. (n = 200); Figure S4. The observed vs. predicted data were estimated using partial least squares regression (PLSR) with hyperspectral reflectance data. The R^2 value was adjusted using a linear equation. Dotted (red) lines represent regression and 1:1, respectively. (n = 50); Figure S5. Observed vs. predicted data estimated by partial least squares regression (PLSR) with hyperspectral transmittance data. The R^2 value was adjusted using a linear equation. The dotted (red) lines represent regression and 1:1, respectively. (n = 50); Figure S6. Observed vs. predicted data estimated by partial least squares regression (PLSR) of hyperspectral absorbance data. The R^2 value was adjusted using a linear equation. The dotted (red) lines represent regression and 1:1, respectively. (n = 50).

Author Contributions: Conceptualisation, R.F.; data curation, R.F. and J.A.M.D.; formal analysis, R.F., W.C.A., J.A.M.D. and M.R.N.; funding acquisition, R.F., R.B.d.O., M.L.C., J.A.M.D. and M.R.N.; investigation, R.F., W.C.A. and M.R.N.; methodology, R.F., R.B.d.O., M.L.C., W.C.A., J.A.M.D. and M.R.N.; project administration, R.F. and M.R.N.; resources, R.F.; software, R.F., R.B.d.O., M.L.C., J.A.M.D. and M.R.N.; supervision, R.F. and M.R.N.; validation, R.F., R.B.d.O., M.L.C., W.C.A. and M.R.N.; visualisation, R.F.; writing—original draft, R.F., R.B.d.O., M.L.C., W.C.A., J.A.M.D. and M.R.N.; writing—review and editing, R.F., R.B.d.O., M.L.C., W.C.A., J.A.M.D. and M.R.N. All authors have read and agreed to the published version of the manuscript.

Funding: National Council for Scientific and Technological Development: Programa de Apoio à Fixação de Jovens Doutores no Brasil 168180/2022−7; Fundação Araucária: CP 19/2022—Jovens Doutores; Coordenação de Aperfeiçoamento de Pessoal de Nível Superior: 001; Fundação de Amparo à Pesquisa do Estado de São Paulo, FAPESP pn 2021/05129−8 for sensor financial support. CEAGRE—Centro de Excelência em Agricultura Exponencial for financial support.

Data Availability Statement: Data are contained within the article and Supplementary Materials.

Acknowledgments: We thank Programa de Pós-Graduação em Agronomia (PGA-UEM) at the State University of Maringá and FAPESP for their support.

Conflicts of Interest: The authors declare no conflicts of interest. The funders had no role in the study design, collection, analyses, interpretation of the data, writing of the manuscript, or decision to publish the results.

References

1. Cotrozzi, L.; Lorenzini, G.; Nali, C.; Pellegrini, E.; Saponaro, V.; Hoshika, Y.; Arab, L.; Rennenberg, H.; Paoletti, E. Hyperspectral Reflectance of Light-Adapted Leaves Can Predict Both Dark- and Light-Adapted Chl Fluorescence Parameters, and the Effects of Chronic Ozone Exposure on Date Palm (*Phoenix dactylifera*). *Int. J. Mol. Sci.* **2020**, *21*, 6441. [CrossRef] [PubMed]
2. Kycko, M.; Zagajewski, B.; Lavender, S.; Dabija, A. In Situ Hyperspectral Remote Sensing for Monitoring of Alpine Trampled and Recultivated Species. *Remote Sens.* **2019**, *11*, 1296. [CrossRef]
3. Vilfan, N.; van der Tol, C.; Muller, O.; Rascher, U.; Verhoef, W. Fluspect-B: A Model for Leaf Fluorescence, Reflectance and Transmittance Spectra. *Remote Sens. Environ.* **2016**, *186*, 596–615. [CrossRef]
4. Ahmed, H.F.A.; Elnaggar, S.; Abdel-Wahed, G.A.; Taha, R.S.; Ahmad, A.; Al-Selwey, W.A.; Ahmed, H.M.H.; Khan, N.; Seleiman, M.F. Induction of Systemic Resistance in *Hibiscus sabdariffa* Linn. to Control Root Rot and Wilt Diseases Using Biotic and Abiotic Inducers. *Biology* **2023**, *12*, 789. [CrossRef] [PubMed]
5. Prabhakara, K.; Dean Hively, W.; McCarty, G.W. Evaluating the Relationship between Biomass, Percent Groundcover and Remote Sensing Indices across Six Winter Cover Crop Fields in Maryland, United States. *Int. J. Appl. Earth Obs. Geoinf.* **2015**, *39*, 88–102. [CrossRef]
6. de Oliveira, M.R.R.; Ribeiro, S.G.; Mas, J.F.; dos Santos Teixeira, A. Advances in Hyperspectral Sensing in Agriculture: A Review. *Rev. Cienc. Agron.* **2020**, *51*, e20207739. [CrossRef]
7. Kior, A.; Sukhov, V.; Sukhova, E. Application of Reflectance Indices for Remote Sensing of Plants and Revealing Actions of Stressors. *Photonics* **2021**, *8*, 582. [CrossRef]
8. Shi, M.; Gu, J.; Wu, H.; Rauf, A.; Emran, T.B.; Khan, Z.; Mitra, S.; Aljohani, A.S.M.; Alhumaydhi, F.A.; Al-Awthan, Y.S.; et al. Phytochemicals, Nutrition, Metabolism, Bioavailability, and Health Benefits in Lettuce: A Comprehensive Review. *Antioxidants* **2022**, *11*, 1158. [CrossRef] [PubMed]
9. Kaňa, R.; Špundová, M.; Ilík, P.; Lazár, D.; Klem, K.; Tomek, P.; Nauš, J.; Prášil, O. Effect of Herbicide Clomazone on Photosynthetic Processes in Primary Barley (*Hordeum vulgare* L.) Leaves. *Pestic. Biochem. Physiol.* **2004**, *78*, 161–170. [CrossRef]
10. Andreeva, A.; Stoitchkova, K.; Busheva, M.; Apostolova, E. Changes in the Energy Distribution between Chlorophyll-Protein Complexes of Thylakoid Membranes from Pea Mutants with Modified Pigment Content. I. Changes Due to the Modified Pigment Content. *J. Photochem. Photobiol. B Biol.* **2003**, *70*, 153–162. [CrossRef] [PubMed]
11. Falcioni, R.; Antunes, W.C.; Demattê, J.A.M.; Nanni, M.R. Biophysical, Biochemical, and Photochemical Analyses Using Reflectance Hyperspectroscopy and Chlorophyll a Fluorescence Kinetics in Variegated Leaves. *Biology* **2023**, *12*, 704. [CrossRef] [PubMed]
12. Cheng, T.; Song, R.; Li, D.; Zhou, K.; Zheng, H.; Yao, X.; Tian, Y.; Cao, W.; Zhu, Y. Spectroscopic Estimation of Biomass in Canopy Components of Paddy Rice Using Dry Matter and Chlorophyll Indices. *Remote Sens.* **2017**, *9*, 319. [CrossRef]
13. Li, K.-Y.; de Lima, R.; Burnside, N.G.; Vahtmäe, E.; Kutser, T.; Sepp, K.; Cabral Pinheiro, V.H.; Yang, M.-D.; Vain, A.; Sepp, K. Toward Automated Machine Learning-Based Hyperspectral Image Analysis in Crop Yield and Biomass Estimation. *Remote Sens.* **2022**, *14*, 1114. [CrossRef]
14. Aneece, I.; Thenkabail, P.S. Classifying Crop Types Using Two Generations of Hyperspectral Sensors (Hyperion and DESIS) with Machine Learning on the Cloud. *Remote Sens.* **2021**, *13*, 4704. [CrossRef]
15. da Silva Junior, C.A.; Nanni, M.R.; Shakir, M.; Teodoro, P.E.; de Oliveira-Júnior, J.F.; Cezar, E.; de Gois, G.; Lima, M.; Wojciechowski, J.C.; Shiratsuchi, L.S. Soybean Varieties Discrimination Using Non-Imaging Hyperspectral Sensor. *Infrared Phys. Technol.* **2018**, *89*, 338–350. [CrossRef]
16. Baio, F.H.R.; Santana, D.C.; Teodoro, L.P.R.; de Oliveira, I.C.; Gava, R.; de Oliveira, J.L.G.; da Silva Junior, C.A.; Teodoro, P.E.; Shiratsuchi, L.S. Maize Yield Prediction with Machine Learning, Spectral Variables and Irrigation Management. *Remote Sens.* **2023**, *15*, 79. [CrossRef]
17. Belwalkar, A.; Poblete, T.; Longmire, A.; Hornero, A.; Hernandez-Clemente, R.; Zarco-Tejada, P.J. Evaluation of SIF Retrievals from Narrow-Band and Sub-Nanometer Airborne Hyperspectral Imagers Flown in Tandem: Modelling and Validation in the Context of Plant Phenotyping. *Remote Sens. Environ.* **2022**, *273*, 112986. [CrossRef]

18. Fernandes, A.M.; Fortini, E.A.; Müller, L.A.d.C.; Batista, D.S.; Vieira, L.M.; Silva, P.O.; do Amaral, C.H.; Poethig, R.S.; Otoni, W.C. Leaf Development Stages and Ontogenetic Changes in Passionfruit (*Passiflora edulis* Sims.) Are Detected by Narrowband Spectral Signal. *J. Photochem. Photobiol. B Biol.* **2020**, *209*, 111931. [CrossRef]
19. Shurygin, B.; Chivkunova, O.; Solovchenko, O.; Solovchenko, A.; Dorokhov, A.; Smirnov, I.; Astashev, M.E.; Khort, D. Comparison of the Non-Invasive Monitoring of Fresh-Cut Lettuce Condition with Imaging Reflectance Hyperspectrometer and Imaging PAM-Fluorimeter. *Photonics* **2021**, *8*, 425. [CrossRef]
20. Jia, M.; Li, D.; Colombo, R.; Wang, Y.; Wang, X.; Cheng, T.; Zhu, Y.; Yao, X.; Xu, C.; Ouer, G.; et al. Quantifying Chlorophyll Fluorescence Parameters from Hyperspectral Reflectance at the Leaf Scale under Various Nitrogen Treatment Regimes in Winter Wheat. *Remote Sens.* **2019**, *11*, 2838. [CrossRef]
21. Sobejano-Paz, V.; Mikkelsen, T.N.; Baum, A.; Mo, X.; Liu, S.; Köppl, C.J.; Johnson, M.S.; Gulyas, L.; García, M. Hyperspectral and Thermal Sensing of Stomatal Conductance, Transpiration, and Photosynthesis for Soybean and Maize under Drought. *Remote Sens.* **2020**, *12*, 3182. [CrossRef]
22. Falcioni, R.; Antunes, W.C.; de Oliveira, R.B.; Chicati, M.L.; Demattê, J.A.M.; Nanni, M.R. Assessment of Combined Reflectance, Transmittance, and Absorbance Hyperspectral Sensors for Prediction of Chlorophyll a Fluorescence Parameters. *Remote Sens.* **2023**, *15*, 5067. [CrossRef]
23. Falcioni, R.; Gonçalves, J.V.F.; de Oliveira, K.M.; de Oliveira, C.A.; Reis, A.S.; Crusiol, L.G.T.; Furlanetto, R.H.; Antunes, W.C.; Cezar, E.; de Oliveira, R.B.; et al. Chemometric Analysis for the Prediction of Biochemical Compounds in Leaves Using UV-VIS-NIR-SWIR Hyperspectroscopy. *Plants* **2023**, *12*, 3424. [CrossRef]
24. Falcioni, R.; dos Santos, G.L.A.A.; Crusiol, L.G.T.; Antunes, W.C.; Chicati, M.L.; de Oliveira, R.B.; Demattê, J.A.M.; Nanni, M.R. Non-Invasive Assessment, Classification, and Prediction of Biophysical Parameters Using Reflectance Hyperspectroscopy. *Plants* **2023**, *12*, 2526. [CrossRef]
25. Asner, G.P.; Jones, M.O.; Martin, R.E.; Knapp, D.E.; Hughes, R.F. Remote Sensing of Native and Invasive Species in Hawaiian Forests. *Remote Sens. Environ.* **2008**, *112*, 1912–1926. [CrossRef]
26. Falcioni, R.; Antunes, W.C.; Demattê, J.A.M.; Nanni, M.R. Reflectance Spectroscopy for the Classification and Prediction of Pigments in Agronomic Crops. *Plants* **2023**, *12*, 2347. [CrossRef] [PubMed]
27. Crusiol, L.G.T.; Nanni, M.R.; Furlanetto, R.H.; Sibaldelli, R.N.R.; Sun, L.; Gonçalves, S.L.; Foloni, J.S.S.; Mertz-Henning, L.M.; Nepomuceno, A.L.; Neumaier, N.; et al. Assessing the Sensitive Spectral Bands for Soybean Water Status Monitoring and Soil Moisture Prediction Using Leaf-Based Hyperspectral Reflectance. *Agric. Water Manag.* **2023**, *277*, 108089. [CrossRef]
28. Boshkovski, B.; Doupis, G.; Zapolska, A.; Kalaitzidis, C.; Koubouris, G. Hyperspectral Imagery Detects Water Deficit and Salinity Effects on Photosynthesis and Antioxidant Enzyme Activity of Three Greek Olive Varieties. *Sustainability* **2022**, *14*, 1432. [CrossRef]
29. Crusiol, L.G.T.; Sun, L.; Sun, Z.; Chen, R.; Wu, Y.; Ma, J.; Song, C. In-Season Monitoring of Maize Leaf Water Content Using Ground-Based and UAV-Based Hyperspectral Data. *Sustainability* **2022**, *14*, 9039. [CrossRef]
30. Crusiol, L.G.T.; Sun, L.; Sibaldelli, R.N.R.; Junior, V.F.; Furlaneti, W.X.; Chen, R.; Sun, Z.; Wuyun, D.; Chen, Z.; Nanni, M.R.; et al. Strategies for Monitoring Within-Field Soybean Yield Using Sentinel-2 Vis-NIR-SWIR Spectral Bands and Machine Learning Regression Methods. *Precis. Agric.* **2022**, *23*, 1093–1123. [CrossRef]
31. Wójtowicz, J.; Grzyb, J.; Szach, J.; Mazur, R.; Gieczewska, K.B. Bean and Pea Plastoglobules Change in Response to Chilling Stress. *Int. J. Mol. Sci.* **2021**, *22*, 11895. [CrossRef] [PubMed]
32. Nalepa, J. Recent Advances in Multi- and Hyperspectral Image Analysis. *Sensors* **2021**, *21*, 6002. [CrossRef] [PubMed]
33. Ge, Y.; Atefi, A.; Zhang, H.; Miao, C.; Ramamurthy, R.K.; Sigmon, B.; Yang, J.; Schnable, J.C. High-Throughput Analysis of Leaf Physiological and Chemical Traits with VIS–NIR–SWIR Spectroscopy: A Case Study with a Maize Diversity Panel. *Plant Methods* **2019**, *15*, 66. [CrossRef] [PubMed]
34. Ferri, C.P.; Formaggio, A.R.; Schiavinato, M.A. Narrow Band Spectral Indexes for Chlorophyll Determination in Soybean Canopies [*Glycine max* (L.) Merril]. *Braz. J. Plant Physiol.* **2004**, *16*, 131–136. [CrossRef]
35. Ling, B.; Goodin, D.G.; Raynor, E.J.; Joern, A. Hyperspectral Analysis of Leaf Pigments and Nutritional Elements in Tallgrass Prairie Vegetation. *Front. Plant Sci.* **2019**, *10*, 142. [CrossRef] [PubMed]
36. Xu, X.; Yang, G.; Yang, X.; Li, Z.; Feng, H.; Xu, B.; Zhao, X. Monitoring Ratio of Carbon to Nitrogen (C/N) in Wheat and Barley Leaves by Using Spectral Slope Features with Branch-and-Bound Algorithm. *Sci. Rep.* **2018**, *8*, 10034. [CrossRef] [PubMed]
37. Thornley, R.H.; Verhoef, A.; Gerard, F.F.; White, K. The Feasibility of Leaf Reflectance-Based Taxonomic Inventories and Diversity Assessments of Species-Rich Grasslands: A Cross-Seasonal Evaluation Using Waveband Selection. *Remote Sens.* **2022**, *14*, 2310. [CrossRef]
38. Pandey, P.; Ge, Y.; Stoerger, V.; Schnable, J.C. High Throughput In Vivo Analysis of Plant Leaf Chemical Properties Using Hyperspectral Imaging. *Front. Plant Sci.* **2017**, *8*, 1348. [CrossRef] [PubMed]
39. Wang, L.; Chang, Q.; Li, F.; Yan, L.; Huang, Y.; Wang, Q.; Luo, L. Effects of Growth Stage Development on Paddy Rice Leaf Area Index Prediction Models. *Remote Sens.* **2019**, *11*, 361. [CrossRef]
40. Fu, Y.; Yang, G.; Song, X.; Li, Z.; Xu, X.; Feng, H.; Zhao, C. Improved Estimation of Winter Wheat Aboveground Biomass Using Multiscale Textures Extracted from UAV-Based Digital Images and Hyperspectral Feature Analysis. *Remote Sens.* **2021**, *13*, 581. [CrossRef]

41. Wang, H.; Mortensen, A.K.; Mao, P.; Boelt, B.; Gislum, R. Estimating the Nitrogen Nutrition Index in Grass Seed Crops Using a UAV-Mounted Multispectral Camera. *Int. J. Remote Sens.* **2019**, *40*, 2467–2482. [CrossRef]
42. Bendig, J.; Bolten, A.; Bennertz, S.; Broscheit, J.; Eichfuss, S.; Bareth, G. Estimating Biomass of Barley Using Crop Surface Models (CSMs) Derived from UAV-Based RGB Imaging. *Remote Sens.* **2014**, *6*, 10395–10412. [CrossRef]
43. Gitelson, A.; Solovchenko, A.; Viña, A. Foliar Absorption Coefficient Derived from Reflectance Spectra: A Gauge of the Efficiency of in Situ Light-Capture by Different Pigment Groups. *J. Plant Physiol.* **2020**, *254*, 153277. [CrossRef] [PubMed]
44. Lichtenthaler, H.K.; Wellburn, A.R. Determinations of Total Carotenoids and Chlorophylls a and b of Leaf Extracts in Different Solvents. *Biochem. Soc. Trans.* **1983**, *11*, 591–592. [CrossRef]
45. Llorach, R.; Martínez-Sánchez, A.; Tomás-Barberán, F.A.; Gil, M.I.; Ferreres, F. Characterisation of Polyphenols and Antioxidant Properties of Five Lettuce Varieties and Escarole. *Food Chem.* **2008**, *108*, 1028–1038. [CrossRef] [PubMed]
46. Ragaee, S. Antioxidant Activity and Nutrient Composition of Selected Cereals for Food Use. *Food Chem.* **2006**, *98*, 32–38. [CrossRef]
47. Zar, J.H. *Biostatistical Analysis*, 5th ed.; Pearson Education: Upper Saddle River, NJ, USA, 2010; ISBN 0-13-100846-3.
48. Pearcy, R.W.; Muraoka, H.; Valladares, F. Crown Architecture in Sun and Shade Environments: Assessing Function and Trade-Offs with a Three-Dimensional Simulation Model. *New Phytol.* **2005**, *166*, 791–800. [CrossRef] [PubMed]
49. Nielsen, S.L.; Nielsen, H.D. Pigments, Photosynthesis and Photoinhibition in Two Amphibious Plants: Consequences of Varying Carbon Availability. *New Phytol.* **2006**, *170*, 311–319. [CrossRef]
50. Yendrek, C.R.; Tomaz, T.; Montes, C.M.; Cao, Y.; Morse, A.M.; Brown, P.J.; McIntyre, L.M.; Leakey, A.D.B.; Ainsworth, E.A. High-Throughput Phenotyping of Maize Leaf Physiological and Biochemical Traits Using Hyperspectral Reflectance. *Plant Physiol.* **2017**, *173*, 614–626. [CrossRef] [PubMed]
51. Saad, A.G.; Pék, Z.; Szuvandzsiev, P.; Gehad, D.H.; Helyes, L. Determination of Carotenoids in Tomato Products Using Vis/NIR Spectroscopy. *J. Microbiol. Biotechnol. Food Sci.* **2017**, *7*, 27–31. [CrossRef]
52. Pontius, J.; Martin, M.; Plourde, L.; Hallett, R. Ash Decline Assessment in Emerald Ash Borer-Infested Regions: A Test of Tree-Level, Hyperspectral Technologies. *Remote Sens. Environ.* **2008**, *112*, 2665–2676. [CrossRef]
53. Apan, A.; Held, A.; Phinn, S.; Markley, J. Formulation and Assessment of Narrow-Band Vegetation Indices from EO-1 Hyperion Imagery for Discriminating Sugarcane Disease. In Proceedings of the 2003 Spatial Sciences Institute Biennial Conference: Spatial Knowledge Without Boundaries (SSC2003), Canberra, Australia, 22–27 September 2003; pp. 1–13.
54. Yoosefzadeh-Najafabadi, M.; Tulpan, D.; Eskandari, M. Using Hybrid Artificial Intelligence and Evolutionary Optimization Algorithms for Estimating Soybean Yield and Fresh Biomass Using Hyperspectral Vegetation Indices. *Remote Sens.* **2021**, *13*, 2555. [CrossRef]
55. Chen, J.; de Hoogh, K.; Gulliver, J.; Hoffmann, B.; Hertel, O.; Ketzel, M.; Bauwelinck, M.; van Donkelaar, A.; Hvidtfeldt, U.A.; Katsouyanni, K.; et al. A Comparison of Linear Regression, Regularization, and Machine Learning Algorithms to Develop Europe-Wide Spatial Models of Fine Particles and Nitrogen Dioxide. *Environ. Int.* **2019**, *130*, 104934. [CrossRef] [PubMed]
56. Wang, D.; Cao, W.; Zhang, F.; Li, Z.; Xu, S.; Wu, X. A Review of Deep Learning in Multiscale Agricultural Sensing. *Remote Sens.* **2022**, *14*, 559. [CrossRef]
57. Thenkabail, P.; Gumma, M.K.; Teluguntla, P.; Ahmed, M.I. Hyperspectral Remote Sensing of Vegetation and Agricultural Crops. *Photogramm. Eng. Remote Sens.* **2014**, *80*, 697–723.
58. Fan, K.; Li, F.; Chen, X.; Li, Z.; Mulla, D.J. Nitrogen Balance Index Prediction of Winter Wheat by Canopy Hyperspectral Transformation and Machine Learning. *Remote Sens.* **2022**, *14*, 3504. [CrossRef]
59. Feng, W.; Yao, X.; Tian, Y.; Cao, W.; Zhu, Y. Monitoring Leaf Pigment Status with Hyperspectral Remote Sensing in Wheat. *Aust. J. Agric. Res.* **2008**, *59*, 748–760. [CrossRef]
60. Nagler, P.L.; Inoue, Y.; Glenn, E.P.; Russ, A.L.; Daughtry, C.S.T. Cellulose Absorption Index (CAI) to Quantify Mixed Soil–Plant Litter Scenes. *Remote Sens. Environ.* **2003**, *87*, 310–325. [CrossRef]
61. Galvão, L.S.; Formaggio, A.R.; Tisot, D.A. Discrimination of Sugarcane Varieties in Southeastern Brazil with EO-1 Hyperion Data. *Remote Sens. Environ.* **2005**, *94*, 523–534. [CrossRef]
62. Prats-Mateu, B.; Felhofer, M.; de Juan, A.; Gierlinger, N. Multivariate Unmixing Approaches on Raman Images of Plant Cell Walls: New Insights or Overinterpretation of Results? *Plant Methods* **2018**, *14*, 52. [CrossRef] [PubMed]
63. Serbin, S.P.; Dillaway, D.N.; Kruger, E.L.; Townsend, P.A. Leaf Optical Properties Reflect Variation in Photosynthetic Metabolism and Its Sensitivity to Temperature. *J. Exp. Bot.* **2012**, *63*, 489–502. [CrossRef] [PubMed]
64. Chicati, M.S.; Nanni, M.R.; Chicati, M.L.; Furlanetto, R.H.; Cezar, E.; De Oliveira, R.B. Hyperspectral Remote Detection as an Alternative to Correlate Data of Soil Constituents. *Remote Sens. Appl. Soc. Environ.* **2019**, *16*, 100270. [CrossRef]
65. Zimmer, G.F.; Santos, R.O.; Teixeira, I.D.; Schneider, R. de C. de S.; Helfer, G.A.; Costa, A. Ben Rapid Quantification of Constituents in Tobacco by NIR Fiber-optic Probe. *J. Chemom.* **2020**, *34*, e3303. [CrossRef]
66. Jensen, J.S.; Egebo, M.; Meyer, A.S. Identification of Spectral Regions for the Quantification of Red Wine Tannins with Fourier Transform Mid-Infrared Spectroscopy. *J. Agric. Food Chem.* **2008**, *56*, 3493–3499. [CrossRef] [PubMed]
67. Zhou, Q.; Yu, L.; Zhang, X.; Liu, Y.; Zhan, Z.; Ren, L.; Luo, Y. Fusion of UAV Hyperspectral Imaging and LiDAR for the Early Detection of EAB Stress in Ash and a New EAB Detection Index NDVI(776,678). *Remote Sens.* **2022**, *14*, 2428. [CrossRef]
68. Iqbal, I.M.; Balzter, H.; Bareen, F.E.; Shabbir, A. Identifying the Spectral Signatures of Invasive and Native Plant Species in Two Protected Areas of Pakistan through Field Spectroscopy. *Remote Sens.* **2021**, *13*, 4009. [CrossRef]

69. Bloem, E.; Gerighausen, H.; Chen, X.; Schnug, E. The Potential of Spectral Measurements for Identifying Glyphosate Application to Agricultural Fields. *Agronomy* **2020**, *10*, 1409. [CrossRef]
70. Ma, Y.; Lee, Y.; Best-Popescu, C.; Gao, L. High-Speed Compressed-Sensing Fluorescence Lifetime Imaging Microscopy of Live Cells. *Proc. Natl. Acad. Sci. USA* **2021**, *118*, e2004176118. [CrossRef] [PubMed]
71. Chen, S.; Zhang, F.; Ning, J.; Liu, X.; Zhang, Z.; Yang, S. Predicting the Anthocyanin Content of Wine Grapes by NIR Hyperspectral Imaging. *Food Chem.* **2015**, *172*, 788–793. [CrossRef] [PubMed]
72. El-Hendawy, S.; Al-Suhaibani, N.; Mubushar, M.; Tahir, M.U.; Marey, S.; Refay, Y.; Tola, E. Combining Hyperspectral Reflectance and Multivariate Regression Models to Estimate Plant Biomass of Advanced Spring Wheat Lines in Diverse Phenological Stages under Salinity Conditions. *Appl. Sci.* **2022**, *12*, 1983. [CrossRef]